



Assembly of a persistent apical actin network by the formin Frl/Fmnl tunes epithelial cell deformability

Benoit Dehapiot¹, Raphaël Clément¹, Hervé Alégot¹, Gabriella Gazsó-Gerhát^{2,3}, Jean-Marc Philippe¹ and Thomas Lecuit^{1,4}✉

Tissue remodelling during *Drosophila* embryogenesis is notably driven by epithelial cell contractility. This behaviour arises from the Rho1-Rok-induced pulsatile accumulation of non-muscle myosin II pulling on actin filaments of the medioapical cortex. While recent studies have highlighted the mechanisms governing the emergence of Rho1-Rok-myosin II pulsatility, little is known about how F-actin organization influences this process. Here, we show that the medioapical cortex consists of two entangled F-actin subpopulations. One exhibits pulsatile dynamics of actin polymerization in a Rho1-dependent manner. The other forms a persistent and homogeneous network independent of Rho1. We identify the formin Frl (also known as Fmnl) as a critical nucleator of the persistent network, since modulating its level in mutants or by overexpression decreases or increases the network density. Absence of this network yields sparse connectivity affecting the homogeneous force transmission to the cell boundaries. This reduces the propagation range of contractile forces and results in tissue-scale morphogenetic defects.

Animal cells can modify their shape to complete complex processes such as cell migration, division or tissue morphogenesis. These behaviours arise from the contractile properties of the actomyosin cortex and its ability to build up tension^{1,2}. Recent advances have shown that cortical contractility can occur in a pulsatile manner by taking the form of local and transient accumulations of myosin II (MyoII)^{3–12}. These MyoII pulses underlie a variety of morphogenetic processes, ranging from single-cell polarization to tissue-scale remodelling. Although recent evidence suggest that MyoII pulsatility can spontaneously emerge^{13–16}, the spatiotemporal pattern of cortical contractility must be controlled to produce reproducible morphogenetic outcomes. In most studied systems, this control is achieved through the conserved RhoA GTPase signalling pathway, which activates MyoII through the regulation of Rho-associated kinase (ROCK; Rok in *Drosophila*) and MyoII light-chain phosphatase^{1,17,18}.

In addition to MyoII regulation, another key parameter that influences cortical contractility resides in the organization and dynamics of the F-actin network. Typically, the cortex assembles as a thin layer of actin filaments bound to the plasma membrane. The cortical network is both highly plastic and mechanically rigid, conferring to the cells the ability to adapt and exert forces on their environment^{2,19–21}. These remarkable properties stem from the action of actin-binding proteins (ABPs) regulating the organization and turnover of the network. Actin nucleators, such as the Arp2/3 complex or formins, promote filament polymerization that leads, respectively, to the assembly of highly branched or sparse F-actin networks. These networks can be remodelled by actin bundlers (fascin and plastin) or cross-linkers (filamin and α-actinin), and their filament turnover regulated by profilin, capping proteins or members of the actin-depolymerizing factor and cofillin families^{19–21}. Modulating the dynamic organization of F-actin networks through

ABPs can significantly modify how MyoII contractility gives rise to cortical tension^{2,22–25}.

In embryonic *Drosophila* epithelial cells, MyoII pulses appear in the medioapical (medial) part of the cell and produce sustained or repeated cycles of apical contraction and relaxation. MyoII pulsatility, together with adherens junction (AJ) remodelling, gives rise to a variety of tissue morphogenetic events such as mesoderm–endoderm invagination, convergent extension or tissue dorsal closure (DC)^{4,7,8}. While the mechanisms underlying the emergence of MyoII pulsatility have been widely studied, little is known about how medioapical F-actin supports pulsatile contractility. It has been shown that the spatiotemporal organization of F-actin modifies the viscoelastic properties of the cortex and its ability to propagate tension²⁶. Cortical F-actin can also influence MyoII activation by serving as a scaffold for the motor-driven advection of regulators such as Rho1, Rok or Rho GTPase-activating proteins (RhoGAPs), which are required for pulse assembly and disassembly^{14,16}. Here, focusing on two highly pulsatile tissues, namely the ectodermal cells during germband extension (GBE) and amnioserosa cells during DC, we studied the regulation of the medioapical F-actin network and sought to understand how it supports the propagation of contractile forces to the surrounding tissue.

Results

Spatiotemporal dynamics of medioapical F-actin. To monitor F-actin dynamics, we stably expressed the actin-binding domain of utrophin fused to enhanced green fluorescent protein (eGFP::UtrCH) in *Drosophila* embryos. This probe allowed the visualization of isolated actin filament without producing artefacts²⁷ (see comparison with phalloidin in Extended Data Fig. 1a). In ectodermal and amnioserosa cells, the medioapical F-actin forms a network of filaments

¹Aix Marseille Université, CNRS, IBDM-UMR7288, Turing Center for Living Systems, Marseille, France. ²Institute of Genetics, Biological Research Centre, HAS, Szeged, Hungary. ³Doctoral School of Biology, Faculty of Science and Informatics, University of Szeged, Szeged, Hungary. ⁴Collège de France, Paris, France. ✉e-mail: thomas.lecuit@univ-amu.fr

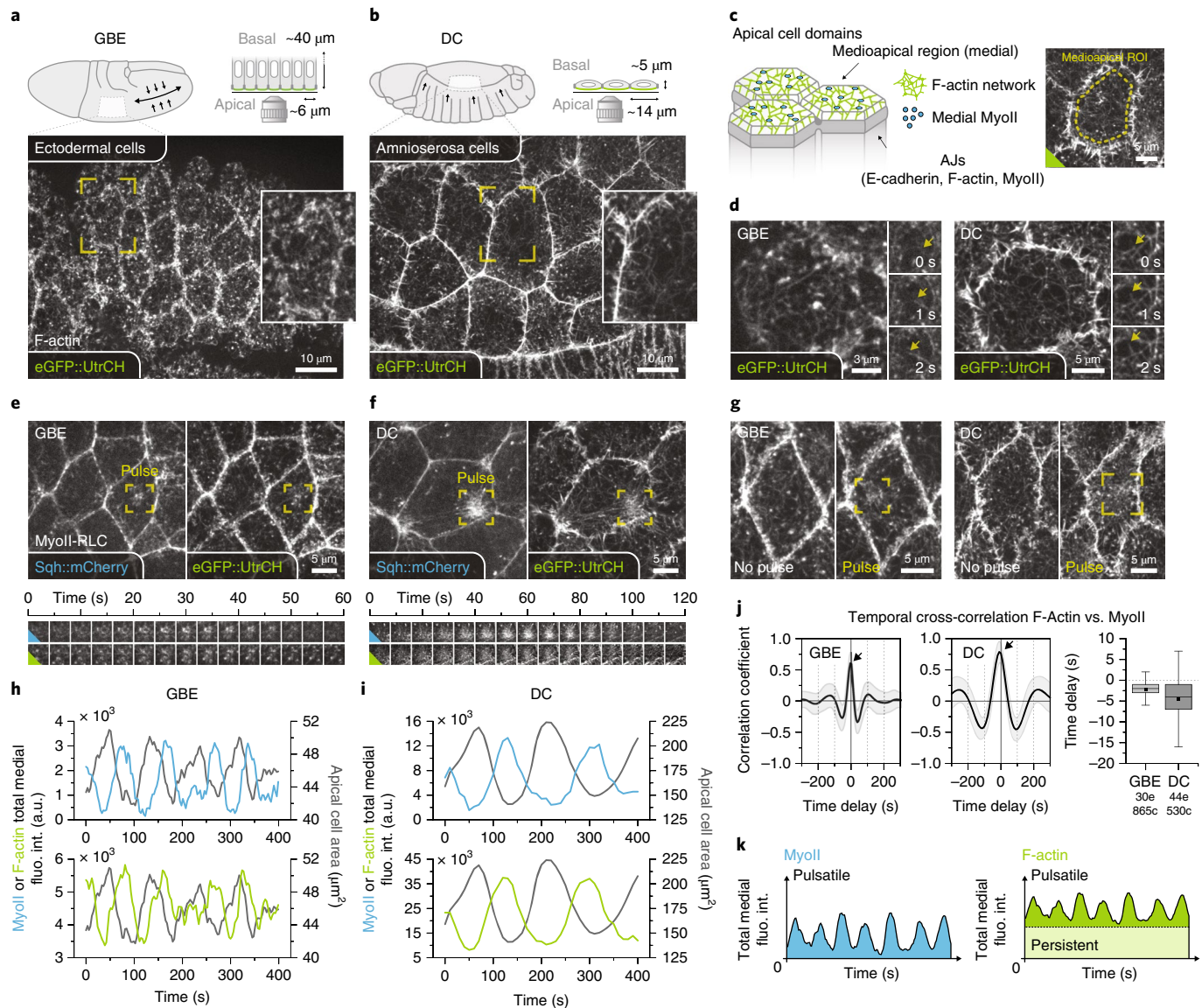


Fig. 1 | Spatiotemporal dynamics of medioapical F-actin. **a,b**, Live imaging of F-actin localization (via eGFP::UtrCH) in ectodermal cells during GBE (a) or amnioserosa cells during DC (b). The upper panels show schematics of cell localizations within the embryo. Main images were extracted from Supplementary Video 1 (GBE; a) or Supplementary Video 2 (DC; b) with the inset zoomed regions indicated by yellow frames. **c**, Left: diagram of the medioapical and junctional subdomains of early *Drosophila* epithelial cells. Right: a typical ROI used to quantify the medioapical actomyosin levels. **d**, High-frequency imaging revealed the medioapical F-actin turnover (eGFP::UtrCH) during GBE and DC. The three images to the right of the main images show time series of actin polymerization events (indicated by yellow arrows). **e,f**, Live imaging of MyoII-RLC (Sqh::mCherry) and F-actin (eGFP::UtrCH) localization during cortical pulsed contractility. Main images (upper) were extracted from Supplementary Video 4 (GBE; e) or Supplementary Video 5 (DC; f). The lower panels are time series of zoomed image sequences showing the assembly-disassembly of a selected actomyosin pulse (indicated by the yellow frames in the upper panels). **g**, Medioapical F-actin (eGFP::UtrCH) localization in cell undergoing (pulse) or not (no pulse) a contractile event during GBE (left) or DC (right). The yellow frames indicate the localization of pulses. **h,i**, Temporal variations of apical area and total medial MyoII-RLC (upper) or F-actin (lower) fluorescence intensity (fluo. int.; given as arbitrary units (a.u.)) in a selected single cell during GBE (h) or DC (i). **j**, Left: line graphs showing the mean \pm s.d. of an averaged temporal cross-correlation analysis between the total medial F-actin and MyoII-RLC fluorescence intensity. Right: box plot of the time delay for maximum correlation (indicated by the black arrows in the line graphs). **k**, Schematic representation of the fluctuation in medial actomyosin levels. Results in a, b and d-i were systematically observed in 50 independent experiments. Results in j are representative of 5 (GBE) and 12 (DC) independent experiments, and quantifications and statistical analyses were performed using $n =$ the total number of cells collected from multiple embryos, as indicated below graphs (e, embryos, c, cells). Box plots extend from the first (Q1) to the third (Q3) quartile (where Q3-Q1 is the interquartile range (IQR)); whiskers are Q1 or Q3 \pm 1.5 \times IQR; horizontal lines represent the median; and black squares represent the mean. Source data are provided.

directly under the apical surface of the cell (Fig. 1a–c). In both tissues, the apical cortex is highly dynamic, displaying contractile foci of F-actin (Supplementary Videos 1 and 2) and a constant turnover of its filaments (Fig. 1d; Supplementary Video 3).

To understand how the cortical dynamics is influenced by MyoII pulsed contractility, we co-expressed the utrophin probe with a tagged version of *Drosophila* MyoII-RLC (Sqh::mCherry or Sqh::mKate2) (Fig. 1e,f; Supplementary Videos 4 and 5). Contrary to

MyoII, the medioapical F-actin network persists between cycles of apical constriction ("no pulse" versus "pulse" in Fig. 1g). Although this observation suggests that the medial F-actin is decoupled from the emergence of pulsed contractility, we also noted that the contractile foci of F-actin correlated with the appearance of MyoII pulses (Fig. 1e,f). To further investigate this phenomenon, we designed an automated cell segmentation and background subtraction procedure to measure the actomyosin levels in the medioapical domain (Methods; Extended Data Fig. 1b,c). By comparing single-cell intensity profiles (Fig. 1h,i) and performing cross-correlation analysis (Fig. 1j), we found that F-actin and MyoII levels are strongly correlated and peak together, with a maximum shift of a few seconds. Since our measurements were carried out on total fluorescence intensities, this suggests that a surge of actin polymerization accompanies the formation of MyoII pulses. These results, consistent with a previous study²⁸, led us to conclude that the medioapical F-actin exhibits two distinct behaviours: first, the assembly of a persistent and homogeneous network and second, the pulsatile polymerization in synchrony with MyoII pulses (Fig. 1k).

Rho1 pathway inhibition reveals two differentially regulated medioapical F-actin subpopulations. To further characterize the mechanisms underlying medioapical F-actin dynamics, we inhibited MyoII pulsatility by targeting the Rho1 signalling pathway (Fig. 2a). We first focused on ectodermal cells during GBE and designed two different strategies to achieve this inhibition. In the first case, we injected the C3 transferase, a well characterized Rho1 inhibitor^{14,29,30}, in pre-gastrulating embryos just before the end of cellularization. This timing allowed the C3 transferase to penetrate the cells (because of its low cell permeability) while not drastically perturbing the early steps of gastrulation. In the second case, we generated maternal and zygotic null-mutant embryos of *RhoGEF2* with germline clones (Methods). *RhoGEF2* encodes a Rho guanine nucleotide exchange factor (RhoGEF) that is the main medioapical Rho1 activator in embryonic *Drosophila* epithelial cells^{31–33}. In both cases, we achieved a complete loss of medial MyoII pulsatility, which resulted in cell and tissue abnormalities (see apical

rounding and reduced AJs in Fig. 2b and Supplementary Video 6). We also noted that the persistent network was preserved in both C3-transferase-injected and *RhoGEF2*^{−/−} embryos (Fig. 2b), since the average medial F-actin density was barely reduced under these inhibitory conditions (Fig. 2c). This shows that the persistent network assembly does not rely on the mechanisms that promote cortical pulsed contractility.

We next tested the impact of Rho1 pathway inhibition on pulsatile F-actin polymerization. To this end, we monitored high-pass-filtered single-cell total fluorescence intensity profiles and quantified the standard deviation as a proxy to measure pulsatility (Fig. 2d,e; Methods and Extended Data Fig. 1d). Following this method, we

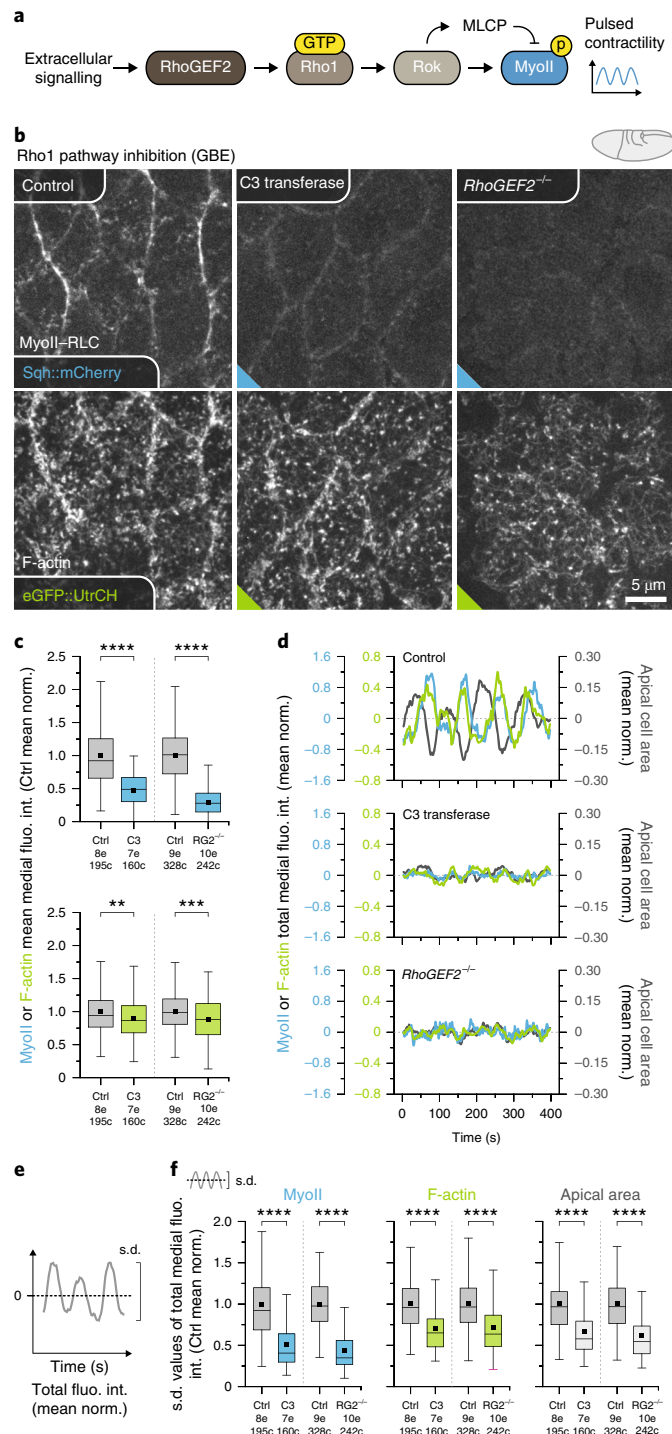


Fig. 2 | Rho1 pathway inhibition reveals two differentially regulated medioapical F-actin subpopulations (GBE). **a**, Simplified schematic of the Rho1 signalling pathway leading to medioapical MyoII activation in early *Drosophila* epithelia. MLCP, MyoII light-chain phosphatase. **b**, Live imaging of MyoII-RLC (Sqh::mCherry; upper) and F-actin (eGFP::UtrCH; lower) localization in ectodermal cells during GBE in control, C3-transferase-injected or *RhoGEF2*^{−/−} mutant embryos. Images were extracted from Supplementary Video 6. **c**, Box plots of the mean medial MyoII (upper) and F-actin (lower) fluorescence intensity averaged per cell and over time (150 × 3 s). Results were normalized to the mean (mean norm.) of controls (Ctrl): water injected (C3 transferase; C3) or WT (*RhoGEF2*^{−/−}; RG2^{−/−}). **d**, Temporal variations in apical cell area (grey), total medial MyoII-RLC and F-actin fluorescence intensity in a selected cell. Data were high-pass filtered and normalized to the mean. **e**, Schematic of measuring the standard deviation (s.d.) of high-pass-filtered apical areas or total medial fluorescence intensity fluctuations as a proxy to quantify pulsatility. **f**, Box plots of cell-averaged s.d. values of high-pass-filtered total medial MyoII-RLC and F-actin fluorescence intensity, and apical area. Results were normalized to the mean of controls. Results in **b–d** and **f** are representative of 11 (7 control, 4 C3 transferase) and 6 (3 control, 3 *RhoGEF2*^{−/−}) independent experiments. Quantifications and statistical analyses in **c** and **f** were performed using n = the total number of cells collected from multiple embryos, as indicated below graphs. Parameters for box plots in **c** and **f** are as described in Fig. 1. Statistics for **c** and **f**: two-sided Mann-Whitney test; **P < 0.005, ***P < 0.0005, ****P < 0.00005. Source data are provided.

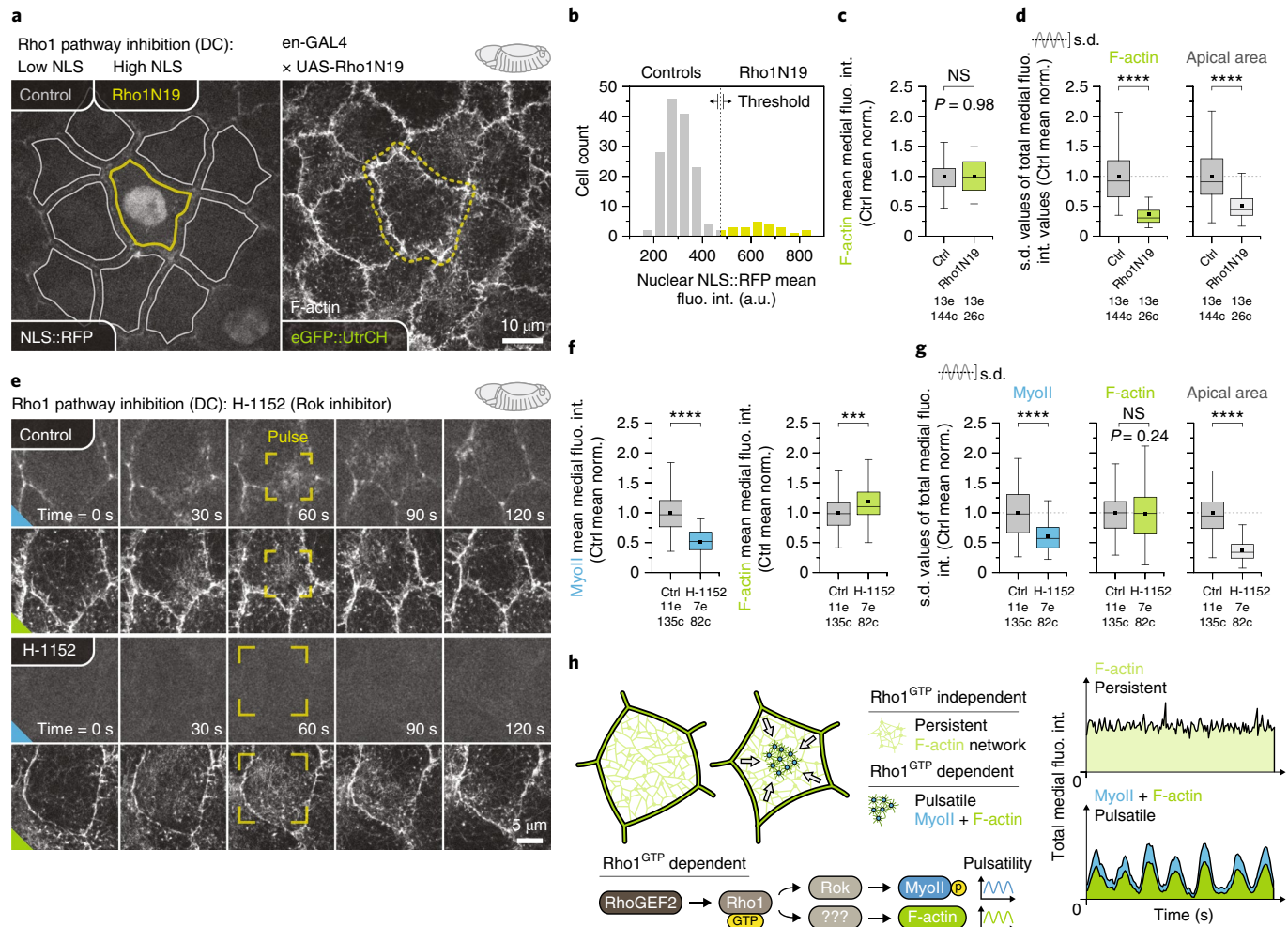


Fig. 3 | Rho1 pathway inhibition reveals two differentially regulated medioapical F-actin subpopulations (DC). **a**, Live imaging of F-actin (eGFP::UtrCH) localization in amniocerosa cells during DC in control (grey outlines) or en-GAL4-induced Rho1N19 (yellow outline) overexpressing cells. Images were extracted from Supplementary Video 7. **b**, Distribution of measured nuclear NLS::RFP fluorescence intensity and selected thresholds to define the control (<475) and Rho1N19 overexpressing cells (>475). **c**, Box plots of the mean medial F-actin fluorescence intensity averaged per cell and over time (90 or 120 × 10 s). Results were normalized to the mean of controls. **d**, Box plots of cell-averaged s.d. values of high-pass-filtered total medial F-actin fluorescence intensity and apical area. Results were normalized to the mean of controls. **e**, Live imaging of MyoII-RLC (Sqh::mKate2; blue triangle) and F-actin (eGFP::UtrCH; green triangle) localization in amniocerosa cells during DC in control (water injected) and H-1152-injected embryos. These time series images were extracted from Supplementary Video 8. The yellow frames show the typical spread of a pulse in these two conditions. **f**, Box plots of the mean medial MyoII and F-actin fluorescence intensity averaged per cell and over time (90 or 120 × 10 s). Results were normalized to the mean of controls. **g**, Box plots of the cell-averaged s.d. values of high-pass-filtered total medial MyoII-RLC and F-actin fluorescence intensities, and apical area. Results were normalized to the mean of controls. **h**, Diagrams representing the differential regulation of medioapical actomyosin. Results in **a–d** are representative of 8 independent experiments. Results in **e–g** are representative of six (three control, three H-1152) independent experiments. Quantifications and statistical analyses in **b–d**, **f** and **g** were performed using n =the total number of cells gathered from multiple embryos, as indicated below the graphs. Parameters of the box plots in **c**, **d**, **f** and **g** are as described in Fig. 1. Statistics in **c**, **d**, **f** and **g**: two-sided Mann-Whitney test, NS, $P > 0.05$, *** $P < 0.0005$, **** $P < 0.00005$. Source data are provided.

found that like the apical cell area and MyoII intensity, the fluctuations of medial F-actin levels were significantly reduced after Rho1-pathway inhibition (Fig. 2f). These results demonstrate that contrary to the persistent network, the pulsatile pool of medial F-actin is chiefly regulated by Rho1 signalling.

In a second step, we investigated whether differential regulation of medioapical F-actin is also present in amniocerosa cells during DC. However, since C3 transferase is not membrane permeable and *RhoGEF2*^{-/-} embryos were unable to reach such a late embryonic stage, we used alternative strategies. We first took advantage of the *engrailed*-GAL4 (en-GAL4) mosaic expression pattern to drive the

overexpression of a Rho1 dominant-negative form, UAS-Rho1N19, in randomly located amniocerosa cells. To identify overexpressing cells, we recombined the en-GAL4 driver with a fluorescent nuclear marker, UAS-NLS::RFP, to act as a reporter (Methods; Fig. 3b). We observed that cells overexpressing Rho1N19 did not undergo pulsed contractility (yellow region of interest (ROI) in Fig. 3a and Supplementary Video 7) contrary to their direct neighbours (same embryo) or cells overexpressing NLS::RFP alone (see control embryos in Extended Data Fig. 3a–c). Strikingly, our quantifications revealed that as in ectodermal cells, only the pulsatile F-actin, and not the persistent network, was perturbed after Rho1

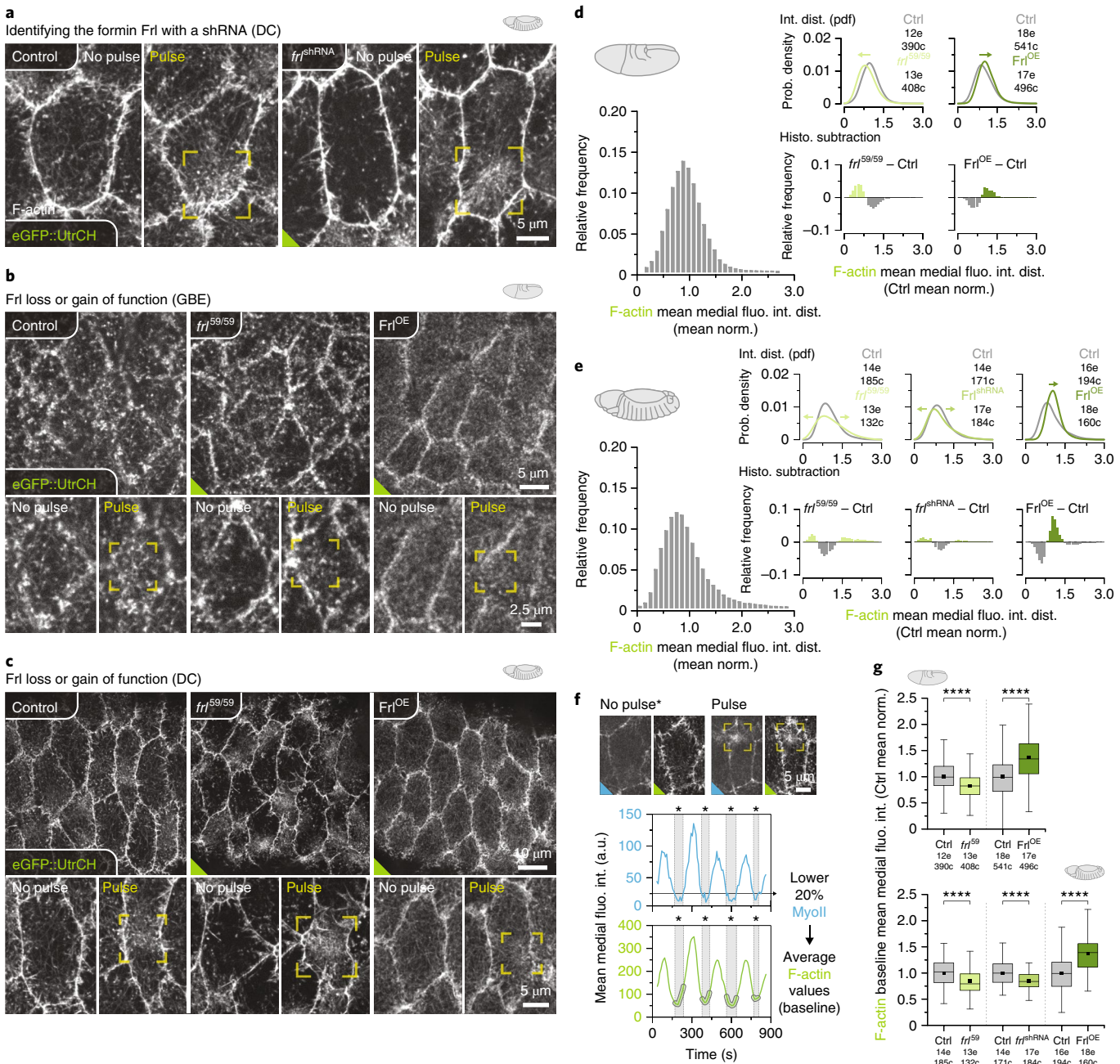


Fig. 4 | The formin Frl promotes the persistent F-actin network assembly. **a–c**, Live imaging of F-actin (eGFP::UtrCH) localization in ectodermal (GBE) and amnirosa cells (DC) in the following conditions: WT, *frl*^{shRNA} (shRNA against Frl), *frl*^{59/59} (*frl* null mutant) or *Frl*^{OE} (Frl overexpression). Images represent either a time point between two pulses ("no pulse") or during a pulse ("pulse") and were extracted from Supplementary Video 9 (DC, WT versus *frl*^{shRNA}) (a), Supplementary Video 10 (GBE, WT versus *frl*^{59/59} versus *Frl*^{OE}) (b) or Supplementary Video 11 (DC, WT versus *frl*^{59/59} versus *Frl*^{OE}) (c). The yellow frames show localization of a pulse. **d,e**, Mean medial F-actin fluorescence intensity distributions (int. dist.) in Frl loss or gain of function during GBE (d) or DC (e). The main bar plots show the distributions for WT embryos. The probability (Prob.) density functions and histograms (Histo.) subtraction showing, respectively, a comparison of the distributions and the relative enrichment of bins between conditions. Distributions are normalized to the mean of controls. **f**, Measurement of the persistent network density (F-actin baseline) by averaging the mean medial F-actin fluorescence intensity during the 20% lowest mean medial MyoII fluorescence intensity time-points. **g**, Box plots of the mean medial F-actin baseline averaged per cell during GBE (upper) or DC (lower). Results were normalized to the mean of controls. For GBE, results in **a–g** are representative of seven (three control, four *frl*^{59/59}) and six (three control, three *Frl*^{OE}) independent experiments. For DC, results in **a–g** are representative of eight (four control, four *frl*^{59/59}), ten (four control, six *frl*^{shRNA}) and eight (four control, four *Frl*^{OE}) independent experiments. Quantifications and statistical analysis in **d–g** were performed using $n =$ the total number of cells gathered from multiple embryos, as indicated below the graphs. Parameters for the box plots in **g** are as described in Fig. 1. Statistics in **g**: two-sided Mann–Whitney test, $****P < 0.00005$. Source data are provided.

inhibition (Fig. 3c,d). These results establish that in both ectodermal and amnirosa cells, the medioapical F-actin network consists of two independently regulated but entangled pools of filaments. On

the one hand, a pulsatile pool of F-actin polymerizing under the control of Rho1 signalling and, on the other hand, a persistent network whose assembly does not depend on this pathway (Fig. 3h).

In a final experiment, we investigated whether the emergence of medial F-actin pulsatility was dependent on MyoII activation. To do so, we inhibited Rok in amnioserosa cells by injecting DC embryos with the cell-permeable H-1152 compound¹⁴. Interestingly, while these injections successfully inhibited MyoII pulses and apical cell contractility, our quantifications revealed that both the persistent and the pulsatile F-actin were preserved in this condition (Fig. 3e–g; Supplementary Video 8). Although pulse dynamics were modified after Rok inhibition (areas framed in yellow in Fig. 3e), we concluded that the emergence, per se, of F-actin pulses does not rely on Rok or MyoII activity (Fig. 3h).

The formin Frl promotes the persistent F-actin network assembly.

Using short hairpin RNA (shRNA) knockdown, we next identified the formin Frl (also known as Fmn1) as a critical factor that promotes the persistent network assembly, since downregulating this formin led to a clear loss of medial F-actin density in the time interval between two MyoII–F-actin pulses (“no pulse” versus “pulse” in Fig. 4a and Supplementary Video 9). This result, alongside the fact that formins promote sparse F-actin networks¹⁹, led us to consider Frl as a good candidate for the assembly of the persistent network.

First, to confirm our loss-of-function phenotype, we used the CRISPR technique to produce a null allele of *frl* (*frl*^{59/59}) (Methods). While this allele caused semi-lethality and semi-sterility, we succeeded to cross homozygote parents (*frl*^{59/59}) and obtained maternal and zygotic null embryos. In a complementary approach, we also studied the effect of a Frl gain of function by overexpressing a UAS-Frl^{WT} construct using a 67-GAL4 driver (condition referred as Frl^{OE}). In both tissues, lowering the Frl levels (*frl*^{59/59} and *frl*^{shRNA}) reduced the density of the persistent network while overexpressing the formin (Frl^{OE}) led to the opposite phenotype (see “no pulse” in Fig. 4a–c and Supplementary Videos 10 and 11). These effects translated into a horizontal shift of the medial F-actin density distributions: towards lower values in Frl loss-of-function conditions and towards higher values in Frl^{OE} embryos (Fig. 4d,e). However, as we further describe below, Frl also influenced the pulsatile pool of F-actin by reducing the amplitude of pulses (the more Frl, the weaker pulses). We therefore designed another quantification method to measure the persistent network density, considering that both the persistent and the pulsatile network account for the measured intensities. To do so, we monitored single-cell MyoII–F-actin profiles and selected the 20% time points for which the MyoII signal was the lowest (Fig. 4f). Considering these time points as inter-pulses period, we averaged the corresponding mean F-actin values (baseline) and observed that in both tissues, lowering the Frl levels reduced the F-actin baseline, while overexpressing Frl produced the opposite effect (Fig. 4g). These results confirm that Frl

plays a pivotal role in the persistent network assembly in ectodermal and amnioserosa cells.

Frl antagonizes Rho1-induced medial pulsed contractility. To better characterize how Frl influences pulsatile F-actin and medio-apical contractility in general, we monitored actomyosin and apical cell area fluctuations (Fig. 5a–d; Supplementary Videos 12 and 13). In amnioserosa cells, the loss of the Frl (*frl*^{59/59}) resulted in a clear increase of both MyoII–F-actin and apical cell area fluctuations, while its overexpression (Frl^{OE}) produced the opposite effect (Fig. 5d). We observed similar tendencies in ectodermal cells, albeit to a lower extent (Fig. 5c). Furthermore, we found that the Frl effect on pulsatility is cell autonomous, since overexpressing the formin in isolated amnioserosa cells (Methods; Fig. 5e–g; Supplementary Video 14) produced similar phenotypes to those observed in a ubiquitous Frl overexpression condition (Figs. 4e and 5d). Taken together, these quantifications show that Frl influences cortical pulsed contractility by counteracting the emergence of actomyosin pulsatility. While additional defects were also observed at cell junctions (Extended Data Fig. 3d,e), these were modest in comparison to the medial apical network modifications (Fig. 4g), which suggests that the latter is probably key to explaining the pulsatility phenotypes.

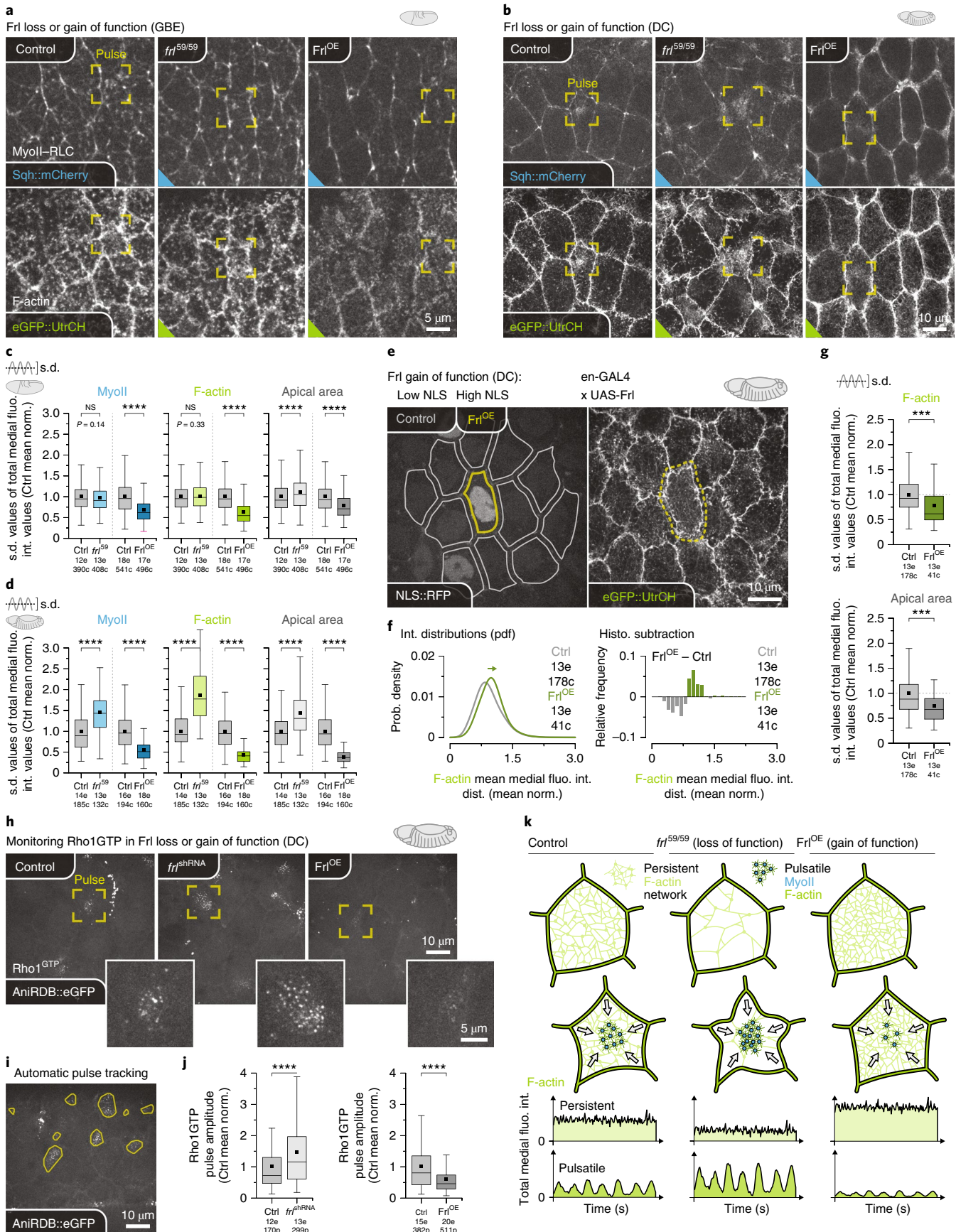
We then asked whether Frl influences actomyosin pulsatility by modulating Rho1 activity. To address this question, we monitored the Rho1-binding domain of anillin fused to eGFP (AniRBD::eGFP) localization in amnioserosa cells. This construct acts as a sensor to follow Rho1 activity since it specifically binds to the GTP-bound form of the GTPase^{14,34}. We next combined the sensor with a 67-GAL4 driver to either overexpress a UAS-driven shRNA (*frl*^{shRNA}) or the UAS-Frl^{WT} construct (Frl^{OE}) (Fig. 5h; Supplementary Video 15). We observed and measured (Methods; Extended Data Fig. 2a; Supplementary Video 16) that reducing Frl levels enhanced the amplitude of AniRBD::eGFP pulses, while overexpressing the formin led to the opposite effect (Fig. 5i,j). This allowed us to conclude that Frl affects apical cell contractility by modulating the levels of Rho1 activation.

Overall, we conclude that tuning Frl levels acts as a switch between two distinct modes of medioapical contractility. At zero or a low level of Frl (*frl*^{59/59} and *frl*^{shRNA}), the persistent network is seriously weakened and actomyosin pulsatility is reinforced. Consequently, cells undergo more pronounced cell shape changes. In sharp contrast, cells overexpressing Frl are more static, showing a low contractility and a dense persistent network (Fig. 5k).

Cellular- and tissue-scale effects of Frl loss or gain of function.

We next wanted to know whether the cellular effects of Frl level

Fig. 5 | Frl antagonizes Rho1-induced medial pulsed contractility. **a,b**, Live imaging of MyoII–RLC (Sqh::mKate2) and F-actin (eGFP::UtrCH) localization in ectodermal (GBE; **a**) and amnioserosa cells (DC; **b**) in WT, *frl*^{59/59} or Frl^{OE} embryos. Images were extracted from Supplementary Video 12 (GBE; **a**) or Supplementary Video 13 (DC; **b**). **c,d**, Box plots of cell-averaged s.d. values of high-pass-filtered total medial MyoII–RLC and F-actin fluorescence intensities, and apical area for ectodermal (GBE; **c**) and amnioserosa (DC; **d**) cells. Results were normalized to the mean of controls. **e**, Live imaging of F-actin (eGFP::UtrCH) localization in amnioserosa cells (DC) in control (grey outlines) or en-GAL4-induced Frl (yellow outline) overexpressing cells. Images were extracted from the Supplementary Video 14. **f**, Probability density functions and histograms subtraction showing, respectively, a comparison of the distributions and the relative enrichment of bins between conditions. Distributions are normalized to the mean of controls. **g**, Box plots of cell-averaged s.d. values of high-pass-filtered total medial F-actin fluorescence intensity and apical area normalized to the mean of controls. **h**, Live imaging of Rho1GTP (AniRBD::eGFP) localization in amnioserosa cells (DC) in WT, *frl*^{shRNA} and Frl^{OE} embryos. Images were extracted from Supplementary Video 15 with the inset zoomed regions indicated by yellow frames. **i**, Representative image of automatic tracking of Rho1GTP pulses (Methods and Supplementary Video 16). **j**, Box plots of the mean Rho1GTP pulse amplitude, normalized to the mean of controls. **k**, Schematic of the effect of modulating Frl levels on medioapical F-actin dynamics. Results in **a** and **c** represent seven (three control, four *frl*^{59/59}) and six (three control, three Frl^{OE}) independent experiments. Results in **b** and **d** represent eight (four control, four *frl*^{59/59}) and eight (four control, four Frl^{OE}) independent experiments. Results in **e–g** represent five independent experiments. Results in **h–j** represent seven (three control, four *frl*^{shRNA}) and ten (five control, five Frl^{OE}) independent experiments. Quantifications and statistical analyses were performed using n =the total number of cells (**c**, **d**, **f** and **g**) or pulses (**j**) collected from multiple embryos, as indicated below the graphs (p, pulses). Parameters for box plots in **c**, **d**, **g** and **j** are as described in Fig. 1. Statistics in **c**, **d**, **g** and **j**: two-sided Mann-Whitney test, NS, $P>0.05$, *** $P<0.0005$, **** $P<0.00005$. Source data are provided.



modification can in turn influence overall tissue dynamics. To answer this question, we first segmented ectodermal cells undergoing convergent extension (GBE) in low-magnification videos (Fig. 6a; Supplementary Video 17). Since convergent extension is driven by cell intercalation (T1 events)^{35–37} and that cell intercalation itself is powered by MyoII pulses^{8,28}, we tracked T1 events and monitored cell area fluctuations as a readout of pulsatility. Our measurements revealed that ectodermal cells intercalate and fluctuate more in *frl*^{59/59} mutants and less in *Frl*^{OE} than in WT embryos (see inserted time projection in Fig. 6a and quantifications in Fig. 6b,c). In general, the occurrence of T1 events and apical cell area fluctuations were positively correlated across conditions (Pearson's coefficient = 0.61, $P=6.1 \times 10^{-6}$; Fig. 6d).

Next, to see how these perturbations influence GBE at the tissue scale, we followed the progression of the posterior midgut (PMG) in differential interference contrast (DIC) videos (Fig. 6e,f; Supplementary Video 18). We observed that an increased occurrence in T1 events (*frl*^{59/59}) had no detectable effect on PMG progression, while, in line with previous studies (for example, mutations in *eve*, *runt* or *Toll2*, *Toll6* and *Toll8*)^{35,38–40}, the latter slowed down when cell intercalation was reduced (*Frl*^{OE}). To further examine this finding, we measured the junction shrinkage and extension rate and found that these two parameters were reduced after *Frl* overexpression, while they were barely modified in the *Frl* loss-of-function condition (Extended Data Fig. 4). The cumulative count of T1 events (Fig. 6g) revealed that the increased number of T1 events observed in *frl*^{59/59} mutants was rather due to an earlier onset of cell intercalation. Interestingly, this early intercalation coincided with faster tissue extension when measured locally (Methods; Fig. 6h). This indicates that although increasing cell intercalation in the *frl*^{59/59} mutants does not accelerate PMG progression, it can, however, facilitate tissue extension at a local scale. Overall, these results suggest that active fluctuations favour T1 events and that *Frl*, by tuning these fluctuations locally, can affect germband dynamics at the tissue scale.

In a second step, we studied how modulating *Frl* levels affects DC. As previously noted, the *frl*^{59/59} phenotype is particularly pronounced in amnioserosa cells, with reinforced actomyosin and apical cell area fluctuations (Fig. 5). We also noted that modulating *Frl* levels changes the way cells deform, with cells in the *frl*^{59/59} condition being more irregularly shaped than in WT and *Frl*^{OE} embryos (Fig. 6i; Supplementary Video 19). Using convex hull (Methods; Fig. 6j), we measured that cells present indeed more inward and outward convolutions in the *Frl* loss-of-function condition than in the other conditions (Fig. 6k).

Although we cannot exclude possible side effects (for example, in the lateral epidermis) of ubiquitous *Frl* loss or gain of function, we

assumed that these local modifications of amnioserosa cells behaviour could underlie the DC defects. Indeed, these cells provide the main forces necessary to complete DC^{41,42}. We therefore imaged *frl*^{shRNA} and *Frl*^{OE} embryos at low magnification, and we observed tissue-scale defects in both conditions (white arrows in Fig. 6l and Supplementary Video 20). We also measured the time elapsed between the end of germband retraction and lateral epidermis closure and found that downregulating *Frl* slows down closure by ~15% (Fig. 6m,n). We were not able to perform such measurements in *Frl*^{OE} embryos due to systematic germband retraction defects. The time delay observed in *frl*^{shRNA} embryos suggests that despite reinforcing pulsatility, lowering *Frl* levels impairs the ability of cells to generate large-scale tissue tension. This could be explained by the fact that reducing the persistent network density leads to an overall decrease of apical cortex stiffness, which is known to increase drastically right at the onset of DC in wild-type (WT) embryos⁴³.

The persistent network promotes the propagation of MyoII-induced contractile forces. The above findings led us to address how the persistent network influences the propagation of contractile forces. To this end, we focused on amnioserosa cells, in which the modulation of *Frl* levels had the strongest phenotype. We observed that pulses tend to contract the entire apical surface in WT cells, while in *frl*^{59/59} cells, they exert contractile forces mostly on their close surroundings (Fig. 7a). This is especially striking when a pulse travels through mutant cells, whereby they only contract nearby AJs (Supplementary Video 21). As a result, pulses in the *frl*^{59/59} mutant generally do not affect the distant parts of the cell, except when sparse radial filaments, emitted by the pulse itself, connect to the AJs (Fig. 7b,c). This can lead to striking deformation dynamics, with distant AJs expanding while nearby AJs are contracting (Fig. 7a). To quantify this effect, we performed an analysis using a KLT tracking algorithm to measure the speed at which tracked apical F-actin structures move towards the pulse as a function of their distance to the pulse (Methods; Fig. 7d; Extended Data Fig. 2b,c; Supplementary Video 22). This allowed us to produce speed propagation curves showing that, in all conditions, speeds were higher near the pulse and decayed gradually with distance (Fig. 7e). However, we observed that the decay length is shorter in *frl*^{59/59} cells, despite higher speeds at close range. This results in a crossover between the *frl*^{59/59} and WT curves. Together, these results suggest that the persistent network promotes the homogeneous and long-range propagation of contractile forces to the cell periphery and the surrounding tissue.

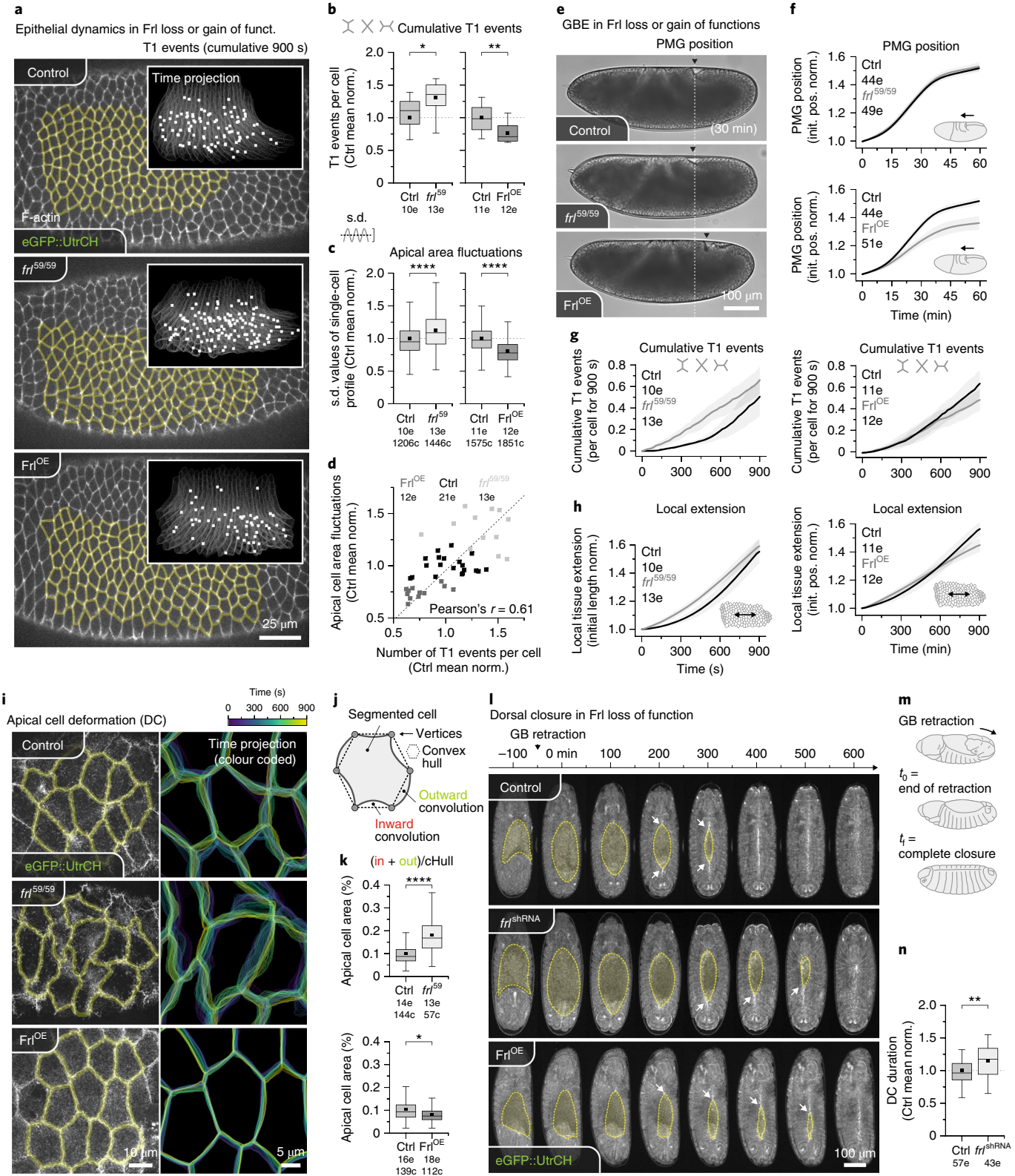
To make sense of these observations, we first hypothesized that heterogeneity of connectivity can reduce the propagation range of contractile forces. We first reasoned that F-actin net-

Fig. 6 | Cellular- and tissue-scale effects of *Frl* loss or gain of function. **a**, Live imaging of F-actin (eGFP::UtrCH) localization in ectodermal cells (GBE) revealing epithelial dynamics in WT, *frl*^{59/59} and *Frl*^{OE} embryos (Supplementary Video 17). Inset images show time projection (900 s) of recorded T1 events (white squares). **b**, Box plots of the number of T1 events per cell, normalized to the mean of controls. **c**, Box plots of cell-averaged s.d. values of high-pass-filtered apical area, normalized to the mean of controls. **d**, Scatter plot of apical area fluctuations versus the number of T1 events per cell. **e**, Live DIC imaging (GBE), extracted 30 min after the onset of gastrulation (Supplementary Video 18). **f**, Averaged PMG position \pm s.d. over time, normalized to the initial PMG position (init. pos. norm.). **g**, Averaged cumulative count of T1 events \pm s.d. over time. **h**, Averaged local tissue extension \pm s.d. over time, normalized to the initial distance. **i**, Live imaging of F-actin (eGFP::UtrCH) in amnioserosa cells (DC) in WT, *frl*^{59/59} and *Frl*^{OE} embryos (Supplementary Video 19). Right images show colour-coded time projection (900 s) of the cell outlines. **j**, Schematic of measuring cell shape irregularity by comparing the convex hull and the segmented apical surface. **k**, Box plots of inward + outward regions over the convex hull (chHull) surface ratio. **l**, Live F-actin (eGFP::UtrCH) low-magnification imaging of embryos undergoing DC in WT, *frl*^{shRNA} and *Frl*^{OE} embryos (Supplementary Video 20). The yellow dashed lines show the amnioserosa cells and the white arrows show the progression of the lateral epidermis closure. **m**, Schematic representation of the DC process. **n**, Box plot of the DC duration normalized to the mean of WT embryos. Results in **a–d**, **g** and **h** represent five (two control, three *frl*^{59/59}) and five (three control, two *Frl*^{OE}) independent experiments. Results in **e** and **f** represent six (two control, two *frl*^{59/59}, two *Frl*^{OE}) independent experiments. Results in **i–k** represent eight (four control, four *frl*^{59/59}) and eight (four control, four *Frl*^{OE}) independent experiments. Results in **l** and **m** represent five (three control, two *frl*^{shRNA}) and six (three control, three *Frl*^{OE}) independent experiments. Quantifications and statistical analyses were performed using n = the total number of embryos (**b**, **d**, **f–h** and **n**) or cells (**c** and **k**) as indicated below the graphs. Parameters for box plots in **b**, **c**, **k** and **n** are as described in Fig. 1. Statistics in **b**, **c**, **k** and **n**: two-sided Mann-Whitney test, * $P < 0.05$, ** $P < 0.005$, *** $P < 0.00005$. Source data are provided.

works behave as a continuous material and that the shorter decay length observed in *frl*^{59/59} cells might result from a reduction of the hydrodynamic length. In a viscoelastic scenario, this distance increases with network stiffness, and the time to propagate over it is typically the dissipation timescale^{20,24,26}. In F-actin networks, dissipation is highly influenced by filament turnover, which occurs over ~10s timescales^{44–46}. However, we did not observe such

contraction delay between distant regions of the cell (Extended Data Fig. 2d), which rules out hydrodynamic length modification as a potential explanation.

We next designed a numerical model in which a randomly positioned pulse applies contractile forces on discretized elements of the cell boundary (Methods; Extended Data Fig. 2e). To consider the variable connectivity of the network, we assumed that the



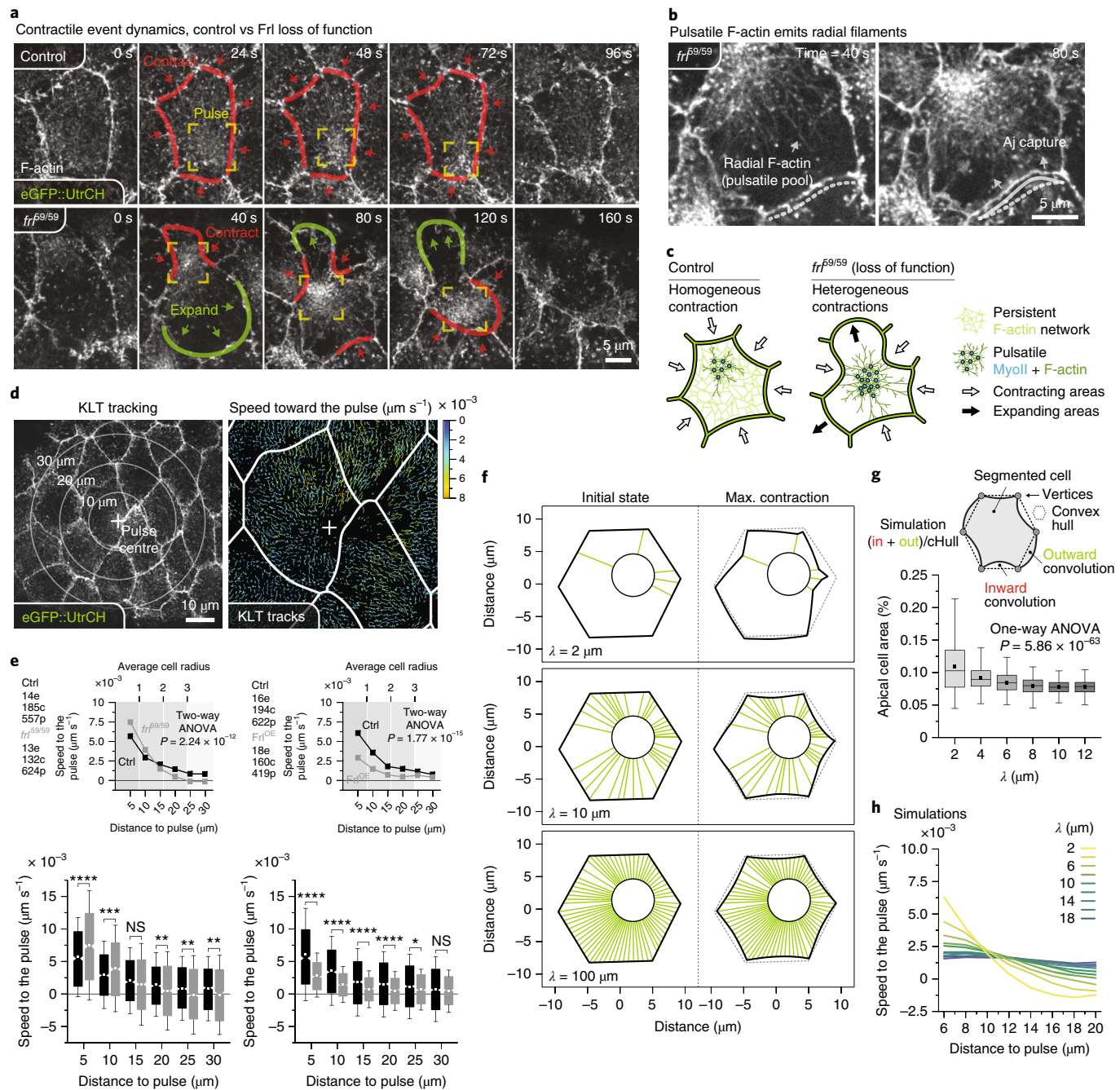


Fig. 7 | The persistent network promotes the propagation of MyoII-induced contractile forces. **a**, Live imaging of F-actin (eGFP::UtrCH) localization in amnioterosa cells (DC) comparing a pulsatile event in a WT and a *frf^{59/59}* cell (Supplementary Video 21). The red and green outlines show, respectively, the contracting and expanding parts of the cell. **b**, Images showing radial F-actin filaments emanating from the pulse in a *frf^{59/59}* cell. The solid and the dashed lines show the contracting AJ. The white arrows indicates actin filaments emanating from the pulse that connect to the AJ. **c**, Schematics of a contracting WT and *frf^{59/59}* cell. **d**, Images of measuring contractile force propagation using KLT tracking (Methods). Left images shows distances from the pulse. Right image shows colour-coded KLT tracks speed towards the pulse (Supplementary Video 22). **e**, Upper: line plots of the means of the binned and averaged speeds towards the pulse versus distance to the pulse. Background shades of grey indicate a typical amnioterosa cell radius (~8 μm). Lower: box plots of the binned and averaged speeds toward the pulse versus the distance to the pulse. **f**, Representative numerical model simulations for different λ values (Supplementary Video 23) with initial condition (left) and maximum deformation (right). Green segments indicate that a boundary element is connected to the pulse. **g**, Schematic and plot of measuring cell shape irregularity by comparing the convex hull and the segmented apical surface. Box plot (simulation) of inward + outward regions over a convex hull surface ratio (200 iterations per λ value). **h**, Line plots (simulation) of averaged speed towards the pulse versus distance to the pulse (200 iterations per λ value). Results in **a** and **b** were systematically observed in 20 independent experiments. Results in **d** and **e** represent eight (four control, four *frf^{59/59}*) and eight (four control, four *Frl^{OE}*) independent experiments. Quantifications and statistical analyses in **e** and **g** were performed using n =the total number of pulses collected from multiple embryos, as indicated below the graphs. Parameters for the box plots in **e** and **g** are as described in Fig. 1. Statistics in **e**: two-sided Mann-Whitney test, NS, $P > 0.05$, * $P < 0.05$, ** $P < 0.005$, *** $P < 0.0005$, **** $P < 0.00005$. Two-way ANOVA in **e** analysed the influence of experimental conditions over the propagation of contractile forces (see interaction P value). One-way ANOVA in **g** analysed the influence of λ over the simulated cell shape deformations. Source data are provided.

probability of an element to be connected to the pulse decays on a length scale λ with the distance d to the pulse, $p \sim e^{-d/\lambda}$. This view is reminiscent of percolation systems in which the size of connected subregions increases with density⁴⁷. Clearly, λ should be small in a low-connectivity regime (*frl*^{59/59} cells) and high when the network density increases (WT and *Frl*^{OE} cells). Our model recapitulated the cell contraction phenotypes observed in the different conditions (Fig. 7f; Supplementary Video 23). When λ is small, force is mostly transmitted to the proximal boundary, which leads to heterogeneous contraction. In contrast, when λ increases, both connectivity and contraction become more homogeneous. As a consequence, lower values of λ result in more convoluted cell shapes, as observed for *frl*^{59/59} cells (Figs. 6i–k and 7g). We also noted that in both simulations and *in vivo* measurements, variability increased when reducing connectivity (low λ or *frl*^{59/59} cells). This is due to the stochastic nature of the low-connectivity regime, in which only a random subset of boundary elements is connected. Indeed, the more boundary elements were connected to the pulse (high λ or *Frl*^{OE} cells), the more reproducible the deformation pattern became (Figs. 6i–k and 7g). Finally, we measured the averaged speed towards the pulse for a wide range of λ values (Fig. 7h), and the observations shown in Fig. 7e were recapitulated, in particular the crossover between propagation curves.

Overall, our results indicate that the persistent F-actin network supports the robust transmission of contractile forces across the apical surface. Absence of this network yields sparse connectivity, which affects the homogeneity of force transmission to AJs and reduces the effective range of contractile forces.

Discussion

While most studies of cortical pulsed contractility have focused on the emergence of MyoII pulsatility, here, we studied how cortical F-actin influences this process in embryonic *Drosophila* epithelial cells. We showed in both ectodermal (GBE) and amnioserosa cells (DC) that the medioapical cortex consists of two differentially regulated but entangled subpopulations of actin filaments. These two populations share the same subcellular localization but undergo distinct spatiotemporal dynamics. The Rho1-induced pulsatile F-actin, together with MyoII, promotes local cell deformations, while the persistent network ensures homogeneous connectivity between pulses and AJs and hence spatial propagation of deformation.

We identified the formin Frl as a critical nucleator that promotes the assembly of the persistent network. This constitutes a previously unappreciated role for this formin, since it has been so far mainly described as participating in lamellipodia and filopodia formation^{48–51}. It would be interesting to know whether, like in other systems, Frl is regulated by Cdc42 (refs. ^{48,51,52}) or Rac1 (ref. ⁵³) to promote the persistent network assembly. Furthermore, it is probable that other formins are involved in this process, since the lack of Frl (*frl*^{59/59}) only partially reduced the network density in ectodermal cells (Fig. 4b). The formin DAAM would constitute a good candidate, since it cooperates with Frl during axon growth in *Drosophila*⁵².

We also showed that Frl antagonizes apical cell contractility by impairing Rho1 signalling in amnioserosa cells. While this antagonism may depend on cell context, it will be interesting to identify the crosstalk mechanisms operating between Frl and the GTPase. To this end, we could draw from previous studies reporting that F-actin can negatively feedback on Rho1 activation^{12,16}. Indeed, it is possible that, like in the *Caenorhabditis elegans* zygote¹⁶, some Rho1 inhibitors (for example, RhoGAPs) bind to cortical F-actin in our systems. Consequently, modifying the persistent network density, through Frl loss or gain of function, could in turn modulate the levels of apical Rho1 activation. It has also been shown that advection acts as a positive feedback for pulsatility by increasing the local concentration of upstream regulators (for example, Rho1 and Rok)¹⁴.

It will therefore be interesting to study how the persistent network influences this feedback mechanism.

Our data also revealed that modulating Frl levels affects epithelial dynamics at the cellular and tissue scales (Fig. 6). Although this is probably influenced by the effect of Frl on medial actomyosin pulsatility and/or MyoII junctional density (Fig. 5), we designed a series of analyses to understand how the persistent network may influence pulsed contractility in mechanical terms. It has been suggested that medioapical F-actin acts as a scaffold to transmit contractile forces to AJs and, by extension, to the surrounding tissue^{8,54–56}. Our results revealed that the persistent network does indeed play a key role in this process by promoting the uniform and long-range propagation of contractile forces. We also devised a numerical model to qualitatively recapitulate our experimental measurements and to provide solid evidence that Frl influences epithelial dynamics through the persistent network.

Tissue morphogenesis requires interactions between cellular- and tissue-scale deformations, the propagation of which in space and time are little understood. We showed here that differentially regulated subpopulations of actin filaments play a key role in this process by promoting distinctly the emergence and the spatial propagation of cortical deformations. Our findings echo previous experimental and theoretical studies demonstrating that the F-actin network, through its cross-linking state^{57–61}, the length of its filaments²⁵ or its turnover⁵⁵, can mediate the amplitude and the length scale at which cortical stresses propagate. It will be important to unravel how cells tune these properties in different tissues and developmental stages to further understand how mechano-chemical information drives embryo morphogenesis.

Online content

Any methods, additional references, Nature Research reporting summaries, source data, extended data, supplementary information, acknowledgements, peer review information; details of author contributions and competing interests; and statements of data and code availability are available at <https://doi.org/10.1038/s41556-020-0524-x>.

Received: 21 June 2019; Accepted: 17 April 2020;

Published online: 1 June 2020

References

- Levayer, R. & Lecuit, T. Biomechanical regulation of contractility: spatial control and dynamics. *Trends Cell Biol.* **22**, 61–81 (2012).
- Salbreux, G., Charras, G. & Paluch, E. Actin cortex mechanics and cellular morphogenesis. *Trends Cell Biol.* **22**, 536–545 (2012).
- Munro, E., Nance, J. & Priess, J. R. Cortical flows powered by asymmetrical contraction transport PAR proteins to establish and maintain anterior-posterior polarity in the early *C. elegans* embryo. *Dev. Cell* **7**, 413–424 (2004).
- Martin, A. C., Kaschube, M. & Wieschaus, E. F. Pulsed contractions of an actin-myosin network drive apical constriction. *Nature* **457**, 495–499 (2009).
- Solon, J., Kaya-Çopur, A., Colombelli, J. & Brunner, D. Pulsed forces timed by a ratchet-like mechanism drive directed tissue movement during dorsal closure. *Cell* **137**, 1331–1342 (2009).
- David, D. J. V., Tishkina, A. & Harris, T. J. C. The PAR complex regulates pulsed actomyosin contractions during amnioserosa apical constriction in *Drosophila*. *Development* **137**, 1645–1655 (2010).
- Blanchard, G. B., Murugesu, S., Adams, R. J., Martinez-Arias, A. & Gorfinkel, N. Cytoskeletal dynamics and supracellular organisation of cell shape fluctuations during dorsal closure. *Development* **137**, 2743–2752 (2010).
- Rauzi, M., Lenne, P. F. & Lecuit, T. Planar polarized actomyosin contractile flows control epithelial junction remodelling. *Nature* **468**, 1110–1115 (2010).
- He, L., Wang, X., Tang, H. L. & Montell, D. J. Tissue elongation requires oscillating contractions of a basal actomyosin network. *Nat. Cell Biol.* **12**, 1133–1142 (2010).
- Kim, H. Y. & Davidson, L. A. Punctuated actin contractions during convergent extension and their permissive regulation by the non-canonical Wnt-signaling pathway. *J. Cell Sci.* **124**, 635–646 (2011).
- Maître, J.-L., Niwayama, R., Turlier, H., Nédélec, F. & Hiragi, T. Pulsatile cell-autonomous contractility drives compaction in the mouse embryo. *Nat. Cell Biol.* **17**, 849–855 (2015).

12. Bement, W. M. et al. Activator–inhibitor coupling between Rho signalling and actin assembly makes the cell cortex an excitable medium. *Nat. Cell Biol.* **17**, 1471–1483 (2015).
13. Dierkes, K., Sumi, A., Solon, J. & Salbreux, G. Spontaneous oscillations of elastic contractile materials with turnover. *Phys. Rev. Lett.* **148**¹⁰², 148102 (2014).
14. Munjal, A., Philippe, J.-M., Munro, E. & Lecuit, T. A self-organized biomechanical network drives shape changes during tissue morphogenesis. *Nature* **524**, 351–355 (2015).
15. Nishikawa, M., Naganathan, S. R., Jülicher, F. & Grill, S. W. Controlling contractile instabilities in the actomyosin cortex. *eLife* **6**, e19595 (2017).
16. Michaux, J. B., Robin, F. B., McFadden, W. M. & Munro, E. M. Excitable RhoA dynamics drive pulsed contractions in the early *C. elegans* embryo. *J. Cell Biol.* **217**, 4230–4252 (2018).
17. Kimura, K. et al. Regulation of myosin phosphatase by Rho and Rho-associated kinase (Rho-kinase). *Science* **273**, 245–248 (1996).
18. Lee, A. & Treisman, J. E. Excessive myosin activity in Mbs mutants causes photoreceptor movement out of the *Drosophila* eye disc epithelium. *Mol. Biol. Cell* **15**, 3285–3295 (2004).
19. Campellone, K. G. & Welch, M. D. A nucleator arms race: cellular control of actin assembly. *Nat. Rev. Mol. Cell Biol.* **11**, 237–251 (2010).
20. Blanchoin, L., Boujemaa-Paterski, R., Sykes, C. & Plastino, J. Actin dynamics, architecture, and mechanics in cell motility. *Physiol. Rev.* **94**, 235–263 (2014).
21. Skau, C. T. & Waterman, C. M. Specification of architecture and function of actin structures by actin nucleation factors. *Annu. Rev. Biophys.* **44**, 285–310 (2015).
22. Reymann, A.-C. et al. Actin network architecture can determine myosin motor activity. *Science* **336**, 1310–1314 (2012).
23. Clark, A. G., Wartlick, O., Salbreux, G. & Paluch, E. K. Stresses at the cell surface during animal cell morphogenesis. *Curr. Biol.* **24**, R484–R494 (2014).
24. Murrell, M., Oakes, P. W., Lenz, M. & Gardel, M. L. Forcing cells into shape: the mechanics of actomyosin contractility. *Nat. Rev. Mol. Cell Biol.* **16**, 486–498 (2015).
25. Chugh, P. et al. Actin cortex architecture regulates cell surface tension. *Nat. Cell Biol.* **19**, 689–697 (2017).
26. Mayer, M., Depken, M., Bois, J. S., Jülicher, F. & Grill, S. W. Anisotropies in cortical tension reveal the physical basis of polarizing cortical flows. *Nature* **467**, 617–621 (2010).
27. Burkel, B. M., Von Dassow, G. & Bement, W. M. Versatile fluorescent probes for actin filaments based on the actin-binding domain of utrophin. *Cell Motil. Cytoskeleton* **64**, 822–832 (2007).
28. Fernandez-Gonzalez, R. & Zallen, J. A. Oscillatory behaviors and hierarchical assembly of contractile structures in intercalating cells. *Phys. Biol.* **8**, 045005 (2011).
29. Nemoto, Y., Namba, T., Kozaki, S. & Narumiya, S. *Clostridium botulinum* C3 ADP-ribosyltransferase gene. *Biol. Chem.* **266**, 19312–19319 (1991).
30. Mason, F. M., Xie, S., Vasquez, C. G., Tworoger, M. & Martin, A. C. RhoA GTPase inhibition organizes contraction during epithelial morphogenesis. *J. Cell Biol.* **214**, 603–617 (2016).
31. Serrano, L., Fernandez-Ballester, G. J., Seher, T., Leptin, M. & Kolsch, V. Control of *Drosophila* gastrulation by apical localization of adherens junctions and RhoGEF2. *Science* **315**, 384–386 (2007).
32. Azevedo, D. et al. DRhoGEF2 regulates cellular tension and cell pulsations in the amnioserosa during *Drosophila* dorsal closure. *PLoS ONE* **6**, e23964 (2011).
33. Kerridge, S. et al. Modular activation of Rho1 by GPCR signalling imparts polarized myosin II activation during morphogenesis. *Nat. Cell Biol.* **18**, 261–270 (2016).
34. Tse, Y. C. et al. RhoA activation during polarization and cytokinesis of the early *Caenorhabditis elegans* embryo is differentially dependent on NOP-1 and CYK-4. *Mol. Biol. Cell* **23**, 4020–4031 (2012).
35. Irvine, K. D. & Wieschaus, E. Cell intercalation during *Drosophila* germband extension and its regulation by pair-rule segmentation genes. *Development* **120**, 827–841 (1994).
36. Bertet, C., Sulak, L. & Lecuit, T. Myosin-dependent junction remodelling controls planar cell intercalation and axis elongation. *Nature* **429**, 667–671 (2004).
37. Blankenship, J. T., Backovic, S. T., Sanny, J. S. S. P., Weitz, O. & Zallen, J. A. Multicellular rosette formation links planar cell polarity to tissue morphogenesis. *Dev. Cell* **11**, 459–470 (2006).
38. Collinet, C., Rauzi, M., Lenne, P.-F. & Lecuit, T. Local and tissue-scale forces drive oriented junction growth during tissue extension. *Nat. Cell Biol.* **17**, 1247–1258 (2015).
39. Lye, C. M. et al. Mechanical coupling between endoderm invagination and axis extension in *Drosophila*. *PLoS Biol.* **13**, e1002292 (2015).
40. Paré, A. C. et al. A positional Toll receptor code directs convergent extension in *Drosophila*. *Nature* **515**, 523–527 (2014).
41. Wells, A. R. et al. Complete canthi removal reveals that forces from the amnioserosa alone are sufficient to drive dorsal closure in *Drosophila*. *Mol. Biol. Cell* **25**, 3552–3568 (2014).
42. Pasarkaris, L., Frei, E., Caussinus, E., Affolter, M. & Brunner, D. Amnioserosa cell constriction but not epidermal actin cable tension autonomously drives dorsal closure. *Nat. Cell Biol.* **18**, 1161–1172 (2016).
43. Ma, X., Lynch, H. E., Scully, P. C. & Hutson, M. S. Probing embryonic tissue mechanics with laser hole drilling. *Phys. Biol.* **6**, 36004 (2009).
44. Fritzsch, M., Lewalle, A., Duke, T., Kruse, K. & Charras, G. Analysis of turnover dynamics of the submembranous actin cortex. *Mol. Biol. Cell* **24**, 757–767 (2013).
45. Bambadekar, K., Clément, R., Blanc, O., Chardès, C. & Lenne, P.-F. Direct laser manipulation reveals the mechanics of cell contacts in vivo. *Proc. Natl. Acad. Sci. USA* **112**, 1416–1421 (2015).
46. Clément, R., Dehapiot, B., Collinet, C., Lecuit, T. & Lenne, P.-F. Viscoelastic dissipation stabilizes cell shape changes during tissue morphogenesis. *Curr. Biol.* **27**, 3132–3142.e4 (2017).
47. Stauffer, D. & Aharonov, A. *Introduction To Percolation Theory* (Taylor & Francis, 1994).
48. Block, J. et al. FMNL2 drives actin-based protrusion and migration downstream of Cdc42. *Curr. Biol.* **22**, 1005–1012 (2012).
49. Kühn, S. et al. The structure of FMNL2–Cdc42 yields insights into the mechanism of lamellipodia and filopodia formation. *Nat. Commun.* **6**, 7088 (2015).
50. Kage, F. et al. FMNL formins boost lamellipodial force generation. *Nat. Commun.* **8**, 14832 (2017).
51. Wakayama, Y., Fukuhara, S., Ando, K., Matsuda, M. & Mochizuki, N. Cdc42 mediates Bmp-induced sprouting angiogenesis through Fmn1-driven assembly of endothelial filopodia in zebrafish. *Dev. Cell* **32**, 109–122 (2015).
52. Dollar, G. et al. Unique and overlapping functions of formins Frl and DAAM during ommatidial rotation and neuronal development in drosophila. *Genetics* **202**, 1135–1151 (2016).
53. Yoshi-Yamamoto, S., Taniguchi, I. & Watanabe, T. FRL, a novel formin-related protein, binds to rac and regulates cell motility and survival of macrophages. *Mol. Cell. Biol.* **20**, 6872–6881 (2002).
54. Levayer, R. & Lecuit, T. Oscillation and polarity of E-cadherin asymmetries control actomyosin flow patterns during morphogenesis. *Dev. Cell* **26**, 162–175 (2013).
55. Jodoi, J. N. et al. Stable force balance between epithelial cells arises from F-actin turnover. *Dev. Cell* **35**, 685–697 (2015).
56. Coravos, J. S. & Martin, A. C. Apical sarcomere-like actomyosin contracts nonmuscle *Drosophila* epithelial cells. *Dev. Cell* **39**, 346–358 (2016).
57. Alvarado, J., Sheinman, M., Sharma, A., MacKintosh, F. C. & Koenderink, G. H. Molecular motors robustly drive active gels to a critically connected state. *Nat. Phys.* **9**, 591–597 (2013).
58. Ennomani, H. et al. Architecture and connectivity govern actin network contractility. *Curr. Biol.* **26**, 616–626 (2016).
59. Stam, S. et al. Filament rigidity and connectivity tune the deformation modes of active biopolymer networks. *Proc. Natl. Acad. Sci. USA* **114**, E10037–E10045 (2017).
60. Ding, W. Y. et al. Plastin increases cortical connectivity to facilitate robust polarization and timely cytokinesis. *J. Cell Biol.* **216**, 1371–1386 (2017).
61. Roh-Johnson, M. et al. Triggering a cell shape change by exploiting preexisting actomyosin contractions. *Science* **335**, 1232–1235 (2012).

Publisher's note Springer Nature remains neutral with regard to jurisdictional claims in published maps and institutional affiliations.

© The Author(s), under exclusive licence to Springer Nature Limited 2020

Methods

Fly strains and genetics. We visualized F-actin dynamics in living embryos using a sqh-eGFP::UtrCH (calponin homology domain of utrophin) insertion either on the second or third chromosome⁶. To co-image F-actin with MyoII, we recombined the eGFP::UtrCH with a fluorescent version of *Drosophila* MyoII-RLC (encoded by the *spaghetti-squash* or *sqh* gene) using a sqh-Sqh::mCherry or a sqh-Sqh::mKate2 insertion. In both cases, these Sqh constructs were inserted either on the K18 site (53B2) on the second chromosome or the VK27 site (89E11) on the third chromosome. To monitor the Rho1 GTPase activity in vivo, we used the Rho1GTP sensor ubi-AnillinRBD::eGFP (Rho binding domain of anillin) inserted on the third chromosome¹⁴.

The 67-GAL4 (mat-4-GAL-VP16) and the en-GAL4 (en2.4-GAL4e16E, UAS-NLS::RFP, Bloomington Drosophila Stock Center (BDSC) no. 30557), carried on the second chromosome, were combined to sqh-eGFP::UtrCH, sqh-Sqh::mKate2 or ubi-AnillinRBD::eGFP on the third chromosome and were used to express the following constructs: UAS-Rho1N19 (BDSC no. 58818), UAS-Frl^{WT} (gift from A. Jenny)⁵² and UAS-*frl*^{shRNA} (CG32138 TRIP line, BDSC no. 32447). The RhoGEF2 germline clones, using the RhoGEF2^{I(2)04291} null allele⁶², were made using the FLP-DFS system⁶³.

To visualize the effect of a ubiquitous overexpression of Frl (Frl^{OE}) in ectodermal cells during GBE we crossed 67-GAL4/+; UAS-Frl^{WT}/+ females with UAS-Frl^{WT}/UAS-Frl^{WT} males (maternal/zygotic Frl overexpression). To visualize the effect of a ubiquitous overexpression of Frl (Frl^{OE}) in amniotserosa cells during DC, we crossed 67-GAL4/67-GAL4;+/+ females with UAS-Frl^{WT}/UAS-Frl^{WT} males (zygotic Frl overexpression). To reduce endogenous Frl levels using shRNA, we crossed 67-GAL4/+/; UAS-*frl*^{shRNA}/+ females with UAS-Frl UAS-*frl*^{shRNA}/UAS-Frl UAS-*frl*^{shRNA} males (maternal/zygotic *Frl* shRNA expression). To drive Rho1N19 or Frl overexpression in isolated amniotserosa cells during DC, we respectively crossed en-GAL4, UAS-NLS::RFP/CyO females with UAS-Rho1N19/CyO or UAS-Frl^{WT}/UAS-Frl^{WT} males (zygotic mosaic expression/overexpression). As a control, we crossed en-GAL4, UAS-NLS::RFP/CyO;+/+ females flies with *yw* males. The nuclear NLS::RFP signal was used as a reporter to identify the isolated amniotserosa cells expressing the en-GAL4 driver. Looking at the distribution of nuclear NLS::RFP intensities, we defined a threshold to categorize cells between controls and overexpressing cells (Fig. 3b). All fly genotypes and crosses are presented in Supplementary Table 1.

Constructs and transgenesis. The *frl*^{F9} mutant was generated using the CRISPR-Cas9 technique⁶⁴. In brief, two 21-nucleotide-long guide RNAs (gRNAs), GAGCAACTTGCCTTATCCGG and GTCGTTTATCGCGCACCTGG, were designed with homology to the second and last coding exons of *frl*, respectively, and cloned into the pCFD4 vector. After germ-cell-specific simultaneous expression of Cas9 and the gRNAs, we collected *frl* mutant candidates from the second generation, which were validated by PCR and sequencing. Based on the sequencing data, the expected ~8,640-bp deletion was detected from the genomic DNA of the mutant strains. We next associated the null *frl*^{F9} allele (third chromosome) with a sqh-eGFP::UtrCH, sqh-Sqh::mKate2 recombinant carried on the second chromosome. From this stock, we selected male and female adult fly homozygotes for *frl*^{F9} and crossed them together to study the effect of maternal and zygotic depletion of Frl on actomyosin dynamics.

Live imaging. Embryos were prepared for live imaging as previously described⁶⁵, and videos were acquired at 22°C at stage 7–8 for ectodermal cells during GBE and at stage 13–14 for amniotserosa cells during DC. All live imaging was performed using a dual camera (QImaging, Rolera EM-C², EMCCD) spinning disc (CSU-X1, Yokogawa) on a Nikon Eclipse Ti inverted microscope (distributed by Roper) managed using the software MetaMorph v7.8.4. Dual colour imaging of eGFP and mCherry/mKate2 fluorescent proteins was obtained by simultaneously exciting fluorophores with a 491-nm and a 561-nm laser and using a dichroic mirror to collect emission signals on two cameras. We used the following Nikon objectives: ×10/numerical aperture (NA) 0.25 dry, ×40/NA 1.25 water and ×100/NA 1.4 oil. For the ×100 videos, we focused on the most apical part of the cell, performing z-series of 1–6 planes separated by 0.33 μm and acquired every 1–10 s (see exact imaging conditions in the legends of the supplementary videos). For epithelial dynamics (×40 videos) (Fig. 6a), we filmed one plane at the AJ level every 20 s. For the ×10 videos (Fig. 6l), we imaged z-series of 10 planes separated by 5 μm every 3 min to capture most of the embryo volume over the duration of the DC process. In all cases, imaging conditions (exposure time and laser power) were optimized and kept constant between controls and perturbed embryos.

Drug injections. To inhibit the Rho1 GTPase in ectodermal cells during GBE, we injected the exoenzyme C3 transferase (Cytoskeleton), resuspended in water at 0.5 μg μl⁻¹, in the yolk of pre-gastrulating embryos. Injections had to be performed just before the end of cellularization to allow this non-cell-permeable drug to penetrate the cells without impairing early gastrulation processes. To inhibit the Rok kinase in amniotserosa cells during DC, we injected the H-1152 compound (Tocris Bioscience), resuspended in water at 40 mM, in the perivitelline space of embryos. In both cases, embryos were slightly dried before injection by exposing them for ~7 min to Drierite (Sigma-Aldrich)

to prevent cells from being expelled from the vitelline shell. Injections were performed using an InjectMan4 micromanipulator and a FemtoJet 4i microinjector from Eppendorf. Embryos were imaged either ~10 min (C3 transferase) or ~2 min (H-1152) after injection.

Embryo fixation and phalloidin staining. To validate the eGFP::UtrCH probe, we compared the live localization of F-actin obtained using this probe to that of fixed embryos stained by phalloidin (Extended Data Fig. 1a). To do so, we fixed embryos in a half-half mix of heptane and 8% paraformaldehyde (diluted in PBS) for 30 min under constant shaking. The embryos were then washed in PBS 10% BSA and hand devitellinized using a thin syringe needle. We next incubated embryos for 2 h at room temperature in a blocking/permeabilizing PBS 10% BSA + 0.3% Triton X-100 solution. OregonGreen 488 phalloidin (Invitrogen) was diluted 1/50 in PBS 10% BSA, and the staining was performed at room temperature for 30 min. Before mounting, the embryos were washed a final time in PBS without BSA. Imaging was performed on a Leica LSM SP8 microscope using a ×100/NA 1.4 oil objective.

Image processing and data analyses. Software. All image processing and data analyses were performed using ImageJ 1.52t or Matlab 2015a either separately or together using the MIJ plugin (D. Sage, D. Prodanov, C. Ortiz and J. Y. Tivenez, retrieved from <http://bigwww.epfl.ch/sage/soft/mij>). The graphics were produced using OriginPro 9.0 software and exported to Adobe Illustrator CS6 for final processing.

Automatic cell segmentation. To measure fluorescence intensities in the medioapical cortex, we first designed an automated cell segmentation procedure based on watershed algorithms (Extended Data Fig. 1b). To achieve this, we used the eGFP::UtrCH signal from the lower planes of our z-series (AJ planes) and reduced the images size ($\times 0.33$) to speed up the procedure. We then ran the DIPIimage watershed algorithm (retrieved from <http://www.diplib.org/dipimage>) and made a custom Matlab/ImageJ code to select and track segmented cells over time. If required, we manually corrected segmentation results using the ImageJ plugin Tissue Analyzer (B. Aigouy, retrieved from <https://grr.gred-clermont.fr/labmirouse/software/WebPA>)⁶⁶.

Image processing and measurements. To prepare the ×100 images for quantification, we first maximum-projected our z-series over two to four of the most apical planes. We then evaluated and subtracted the cytoplasmic background by measuring fluorescence intensities on the lower z-planes (Extended Data Fig. 1c). This step was critical to properly monitor the total amount of fluorescence in the ever-changing apical cell surface without introducing bias (for example, temporal shift) in the measurements. We next quantified the medioapical fluorescence intensities using segmented ROIs, reduced by 10 or 15 pixels (for ectodermal and amniotserosa cells, respectively), to prevent the junctional signal from contaminating the measurements. Alternatively, we measured the junctional fluorescence intensities (Extended Data Fig. 3d, e) using the same ROIs, but this time by expanding the contours by 3 pixels. According to the experiment, we either measured the mean or the integrated medial fluorescence intensities to get information about the density or the total levels, respectively, of the considered fluorescent protein.

Measuring the level of pulsed contractility. During this study, we repeatedly assessed the level of pulsed contractility by comparing the medial actomyosin pulsatility and the apical cell area fluctuations (Figs. 2f, 3d,g, 5c,d,g and 6c). To do so, we measured the standard deviations of mean-normalized individual cell profiles for which we removed the low-frequency components using an IIR Butterworth high-pass filter (Matlab signal processing toolbox). We choose a 1/300 s (ectodermal cells) or 1/600 s (amniotserosa cells) cut-off frequency and multiplied it by 0.75 or 1.25 to define the stop and the pass band frequency, respectively (Extended Data Fig. 1d). The high-pass filter allowed us to isolate the effect of pulsed contractility by discarding the slow variations of the apical surface. Removing the low-frequency components was mandatory to measure the F-actin pulsatility since the total amount of medial filaments tend to scale with the apical cell surface.

Cross-correlation analysis. To evaluate how the pulsatile F-actin accumulations synchronize with the MyoII pulses, we performed a cross-correlation analysis by comparing mean-normalized and high-pass-filtered (see above) total medial F-actin and MyoII level variations (Fig. 1j). The normalized cross-correlation (C) was calculated for individual cells using the following formula, where t is the time, T is the total time of analysis and τ is the time delay:

$$C_N(\tau) = \frac{\int_0^T (f(t) - \bar{f}) \times (g(t + \tau) - \bar{g}) dt}{\sqrt{\int_0^T (f(t) - \bar{f})^2 dt} \times \sqrt{\int_0^T (g(t) - \bar{g})^2 dt}}$$

The presented cross-correlation curves were obtained by averaging individual cell results, and the typical time delays were plotted considering the maximum correlation for the F-actin and MyoII comparisons.

Quantifying pulsatile Rho1 activity. To quantify the levels of Rho1 activity during pulses, we measured the amplitude of AniRBD::eGFP (Rho1GTP sensor) accumulations during contractile events (Fig. 5h–j). However, since we were unable to segment cells using the AniRBD::eGFP signal, we designed a live pulse tracking procedure that worked directly on unsegmented images (Extended Data Fig. 2a). To do so, we used a Matlab implementation of the DBSCAN clustering algorithm (S. Mostapha Kalam Heris, retrieved from <http://yarpiz.com/255/ypml10-dbscan-clustering>) integrated to a custom code for automatization. This method allowed us to isolate clusters of AniRBD::eGFP signal based on two main parameters: the distance ϵ and the minimum number of points that must be within an ϵ radius for these points to be considered as a cluster. We then converted these clusters into ROIs, using convex hulls (minimum area polygon containing the cluster), and tracked overlapping ROIs over time to follow individual pulses. After filtering pulses, based on ROI sizes and tracks duration criterions, we measured the amplitude of AniRBD::eGFP pulses by measuring the maximum of total fluorescence intensity for each track.

Tissue-scale dynamics during GBE. To monitor T1 events during GBE (Fig. 6a,b,d,g), we used the stable T1 tracker included with the ImageJ plugin Tissue Analyzer (B. Aigouy, retrieved from <https://grr.gred-clermont.fr/labmirouse/software/WebPA>)⁶⁶. The tracker automatically detects cells losing contact in an irreversible manner. We then wrote a custom Matlab code to automatically extract the spatiotemporal localization of intercalating cells. We also used Tissue Analyzer combined with another Matlab routine to measure the length and orientation of shrinking and extending AJs defined as disappearing and appearing, respectively, junctions (Extended Data Fig. 4). To measure the rate of shrinkage and extension, we linearly fitted the last 5 min before and the first 5 min after the four-way vertex stage. Finally, we quantified total tissue extension (Fig. 6g) by measuring over time the distance between the centroid of two distant groups of cells (defined as the 10 left-most and the 10 right-most cells on $\times 40$ videos).

Cell shape regularity measurements (DC). To measure cell shape regularity, we compared the segmented cell boundary with the convex hull formed by connecting vertices (Figs. 6i–k and 7g). We next quantified the area occupied by the inward-outward convolutions of the actual cell shape and divided it by the surface of the convex hull. In doing so, we obtained a ratio whose value indicates the convolution level of the segmented cell shape (the higher the value, the more convoluted the shape). We calculated this ratio for every cell at every time point and then compared it between conditions.

KLT and pulse analysis. To measure the cortical propagation of MyoII-induced pulsatile stresses, we quantified the speed at which discrete apical F-actin structures (eGFP::UtrCH signal) displace towards the pulse centre during contractile events.

To define the pulse centre, we first detected pulses in time using the function “findpeaks” in Matlab (Signal Processing Toolbox) on smoothed and high-pass-filtered total MyoII intensity profiles (Extended Data Fig. 2b). Combined with a derivative analysis, this allowed us to define temporal landmarks within pulses (t_i : initial time; $t_{d\max}$: max derivative; t_{\max} : max amplitude; $t_{d\min}$: min derivative; t_f : final time). We next implemented another Matlab routine to monitor the medial MyoII centre of mass within contracting cells (Extended Data Fig. 2c). To do this, we applied a combination of Gaussian blurs and thresholding steps to isolate the MyoII signal actually belonging to the pulse. Finally, we combined these two approaches and used the averaged position of the MyoII centre of mass, between the $t_{d\max}$ and $t_{d\min}$, as our reference pulse centre.

To track discrete apical F-actin structures, we used a KLT features tracking algorithm implemented in the C programming language^{67,68} coupled with an affine consistency test to minimize errors⁶⁹ (S. Birchfield, retrieved from <https://cecas.clemson.edu/~stb/klt>). Due to the constant reorganization of medial F-actin, we replaced lost tracks at each time point and obtained an average of 50,000 tracks (≥ 3 time points) per embryo.

Finally, we produced propagation curves (Fig. 7e) by averaging the speed, between $t_{d\max}$ and $t_{d\min}$, at which KLT-tracked structures converged towards the pulse centre. We then binned data according to the distance and plotted the measured speed towards the pulse as a function of the distance to the pulse.

Numerical modelling. We consider a single cell subjected to a contraction due to an actomyosin pulse. The cell contour is discretized with N attachment sites ($N=100$). Six sites represent the vertices. Initially, sites are regularly distributed along the contour. They are subjected to the following forces:

- An area constraint in the form of cell area elasticity as follows:

$$\vec{F}_A = -k_A(A - A_0)\vec{u}_r$$

where k_A is the area stiffness (that is, the strength associated to the area constraint), A is the area of the cell, A_0 its target area and \vec{u}_r the unit radial vector. The origin is taken at the cell centre of mass.

- A line tension along the cell contour. The site i pulls on the neighbouring sites $i-1$ and $i+1$ as follows:

$$\vec{T}_{i,i\pm 1} = -\gamma l_{i,i\pm 1}\vec{u}_{i,i\pm 1}$$

where γ is the line tension constant, $l_{i,i\pm 1}$ is the distance between sites i and $i\pm 1$ and $\vec{u}_{i,i\pm 1}$ is the unit vector along the segment joining sites i and $i\pm 1$.

- A traction from adjacent cell junctions on vertices is mimicked via an additional elastic force acting only on vertices sites as follows:

$$\vec{F}_v = -k_v l_v \vec{u}_v$$

where k_v is the strength associated to the elastic force, l_v is the distance of the vertex to its initial position and \vec{u}_v is the unit vector along the segment joining the vertex to its initial position.

- An active contraction force distributed among the connected attachment sites. The contraction force on site i is as follows:

$$\vec{F}_c^i = -\chi_i C(t) \vec{u}_p^i$$

where χ_i is either 1 or 0 (connected or not, see below), $C(t)$ is the amplitude of the contraction force and \vec{u}_p^i is the unit vector along the segment joining site i to the pulse centre. In each simulation, the position of the pulse centre is randomly chosen anywhere inside the cell. The probability that a contour site is connected to the pulse depends on its distance d_i to the pulse as follows:

$$p_i = e^{-d_i/\lambda}$$

where λ is a connectivity length scale and a direct indicator of network density. A sparse network will result in a short λ , while a dense network will result in a long λ . We consider that the pulse has a non-zero spatial extension with radius r_p . The probability that an attachment site within the pulse radius is connected to the pulse is equal to 1. Hence the distance d_i is computed as the distance to the pulse circumference.

The amplitude of the contraction force $C(t)$ is as follows:

$$C(t) = \frac{C_0}{N_c} \frac{1}{2} (1 - \cos(2\pi t/\theta))$$

The amplitude on each site C_0/N_c is normalized to the number of connected sites N_c so that the total work produced does not depend on the number of connected sites. We assumed that the contraction amplitude oscillates with period θ . Due to the periodicity, we limited the simulations to one period.

The dynamics were simulated by solving the force balance equation, assuming a fluid friction force with friction coefficient α as follows:

$$\frac{d\vec{x}_i}{dt} = \frac{1}{\alpha} (\vec{F}_A^i + \vec{T}_i + \vec{F}_v^i + \vec{F}_c^i)$$

We used $A_0 = 170 \mu\text{m}^2$, $r_p = 3.5 \mu\text{m}$, $\theta = 200 \text{ s}$, $\gamma = 120$, $\alpha = 5$, $k_A = 0.05$, $k_v = 30$ and $C_0 = 500$. The initial (equilibrium) configuration before the contraction starts is a hexagon. We used different values of λ , ranging from $2 \mu\text{m}$ to $100 \mu\text{m}$, to illustrate the role of connectivity. For the propagation curves (Fig. 7h), we plotted the velocity of the attachment sites as a function of their distance to the pulse. Because the model is limited to a single cell, it can only treat distances up to a cell diameter (typically $20 \mu\text{m}$).

Statistics and reproducibility. Data points from different pulses, cells and embryos were pooled to estimate the mean and standard deviations. The quantifications were carried out on a minimum number of seven embryos from a minimum number of three independent experiments (mounting). No embryos were excluded from analyses. In general, statistical significance was tested using Mann–Whitney tests, assuming non-normal distributions and equal variances. For the data in Fig. 7e, we performed a two-way analysis of variance (ANOVA) to test the influence of experimental conditions over the propagation of contractile forces (see interaction P value). For the data in Fig. 7g, we performed a one-way ANOVA to test the influence of the λ parameter over the simulated cell shape deformations. No statistical method was used to predetermine sample sizes. The experiments were not randomized, and the investigators were not blinded to allocation during experiments and outcome assessment.

Reporting Summary. Further information on research design is available in the Nature Research Reporting Summary linked to this article.

Data availability

All data, such as raw images, supporting the findings of this study are available from the corresponding author upon reasonable request. Source data for Figs. 1–7 and Extended Data Figs. 1–4 are presented with the paper.

Code availability

Codes and plugins used in this study can be retrieved as referenced in the Methods section of the manuscript. All other custom codes are available from the corresponding author upon reasonable request.

References

62. Häcker, U. & Perrimon, N. DRhoGEF2 encodes a member of the Dbl family of oncogenes and controls cell shape changes during gastrulation in *Drosophila*. *Genes Dev.* **12**, 274–284 (1998).
63. Chou, T. Bin & Perrimon, N. The autosomal FLP-DFS technique for generating germline mosaics in *Drosophila melanogaster*. *Genetics* **144**, 1673–1679 (1996).
64. Gratz, S. J. et al. Genome engineering of *Drosophila* with the CRISPR RNA-guided Cas9 nuclease. *Genetics* **194**, 1029–1035 (2013).
65. Cavey, M. & Lecuit, T. In *Drosophila: Methods and Protocols* (ed. Dahmann, C.) 219–238 (Humana Press, 2008).
66. Aigouy, B. et al. Cell flow reorients the axis of planar polarity in the wing epithelium of *Drosophila*. *Cell* **142**, 773–786 (2010).
67. Lucas, B. D. & Kanade, T. An iterative image registration technique with an application to stereo vision. In *Proc. 7th International Joint Conference on Artificial Intelligence—Volume 2* 674–679 (Morgan Kaufmann Publishers, 1981).
68. Tomasi, C. & Kanade, T. Detection and tracking of point features. *Int. J. Comput. Vis.* **9**, 137–154 (1991).
69. Shi, J. & Tomasi, C. Good Features to track. In *IEEE Conf. Comput. Vis. Pattern Recognit.* (IEEE, 1994).

Acknowledgements

We are grateful to J. Mihály (Biological Research Centre, HAS, Szeged, Hungary) and A. Jenny (Albert Einstein College of Medicine, The Bronx, NY, USA) for providing fly stocks. We thank members of the Lecuit and Lenne groups for stimulating discussions and comments during the course of this project. We also thank FlyBase for maintaining databases and the Bloomington Drosophila Stock Center for providing fly stocks. The experiments were performed using the PiCSL-FBI core facility (IBDM, Marseille, France), a member of the France-BioImaging national research infrastructure supported by the French National Research Agency (ANR-10-INBS-04-01, “Investissements d’Avenir”). B.D. was supported by the ERC Biomecamorph (grant no. 323027) and Fondation Bettencourt Schueller. R.C. and J.-M.P. were supported by the CNRS. H.A. was supported by the ANR MechaResp (ANR-17-CE13-0032). T.L. was supported by the CNRS, followed by the Collège de France.

Author contributions

B.D. and T.L. conceived the project. B.D. performed experiments and quantifications and developed analytical methods. R.C. designed the numerical model and performed the simulations. H.A. performed the experiments presented in Supplementary Fig. 3a–c and Fig. 6*l* (*Frl*^{OE}). G.G.-G. isolated the *frl*^{P99} null allele. J.-M.P. created all the fluorescent constructs. B.D., R.C. and T.L. discussed the data and wrote the manuscript.

Competing interests

The authors declare no competing interests.

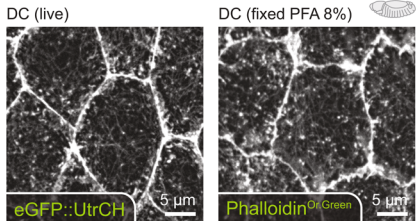
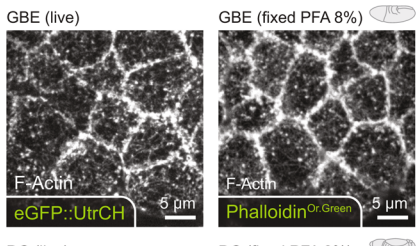
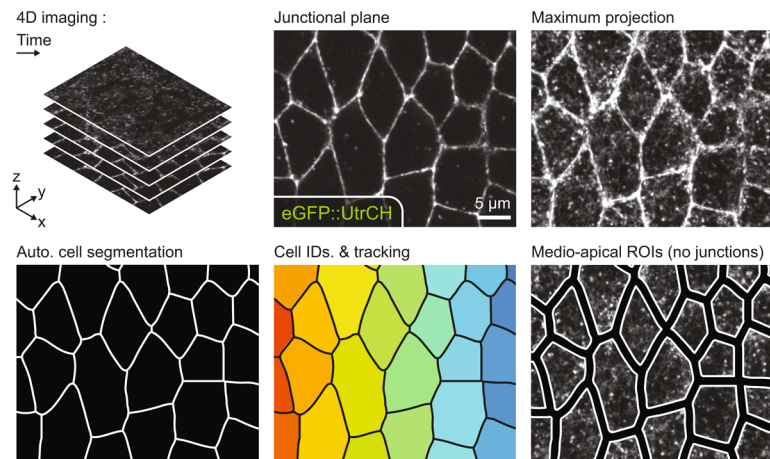
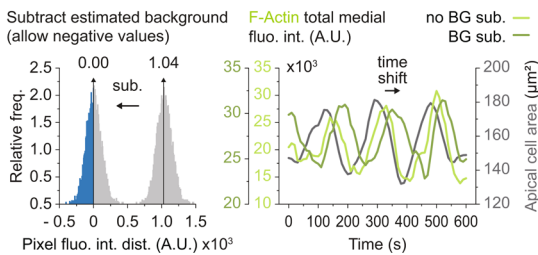
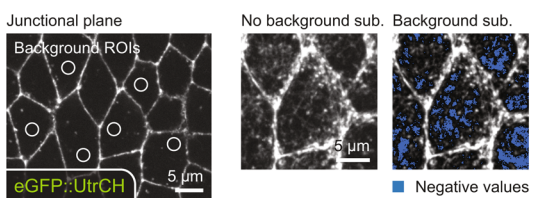
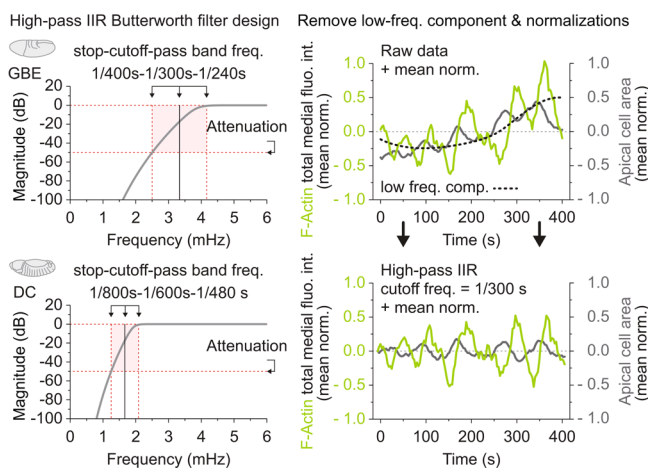
Additional information

Extended data is available for this paper at <https://doi.org/10.1038/s41556-020-0524-x>.

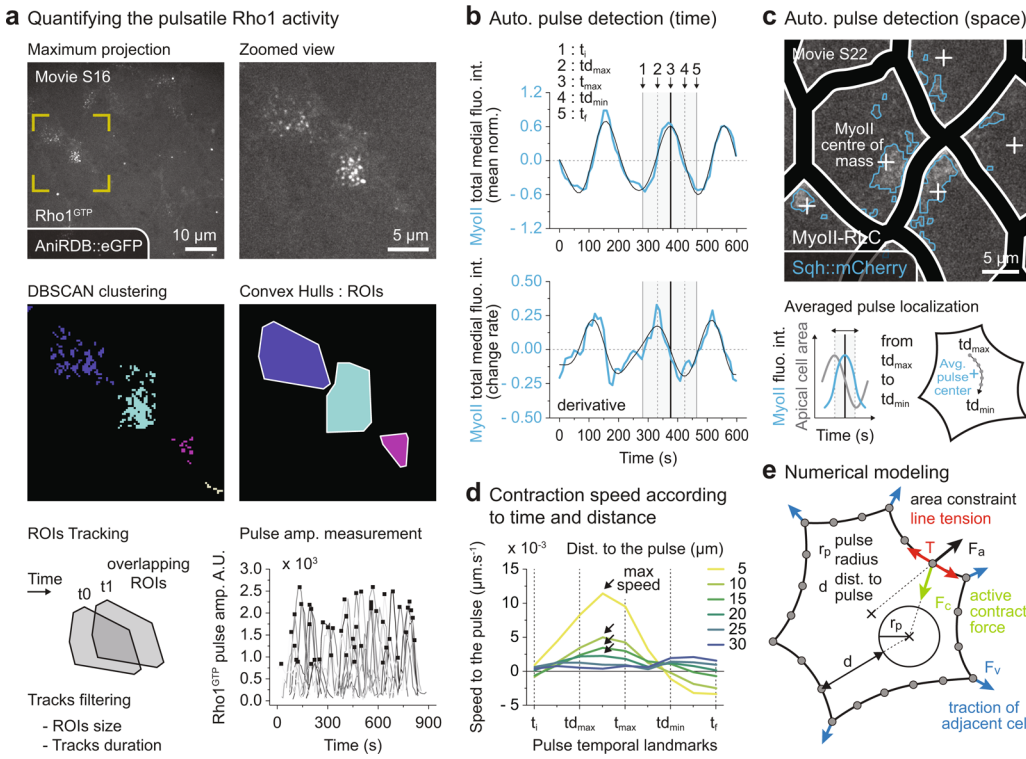
Supplementary information is available for this paper at <https://doi.org/10.1038/s41556-020-0524-x>.

Correspondence and requests for materials should be addressed to T.L.

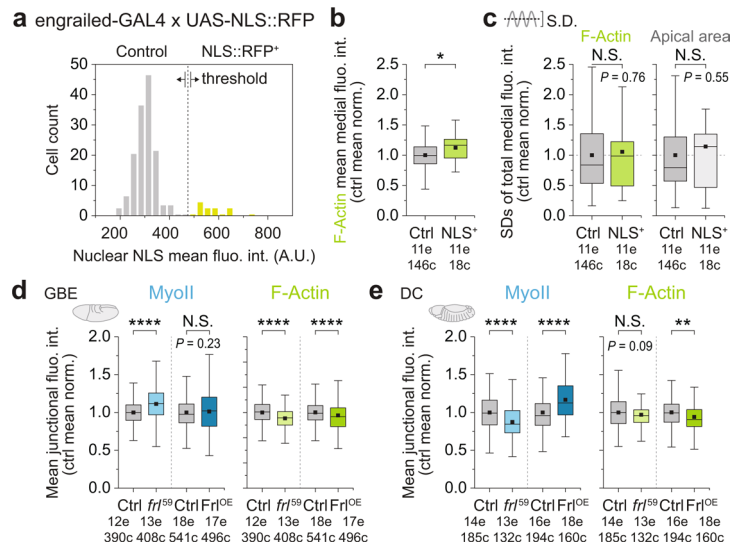
Reprints and permissions information is available at www.nature.com/reprints.

a Monitoring F-Actin in vivo using eGFP::UtrCH**b** Automatic cell segmentation & medio-apical ROIs**c** Estimate & subtract background**d** Measuring the level of pulsed contractility

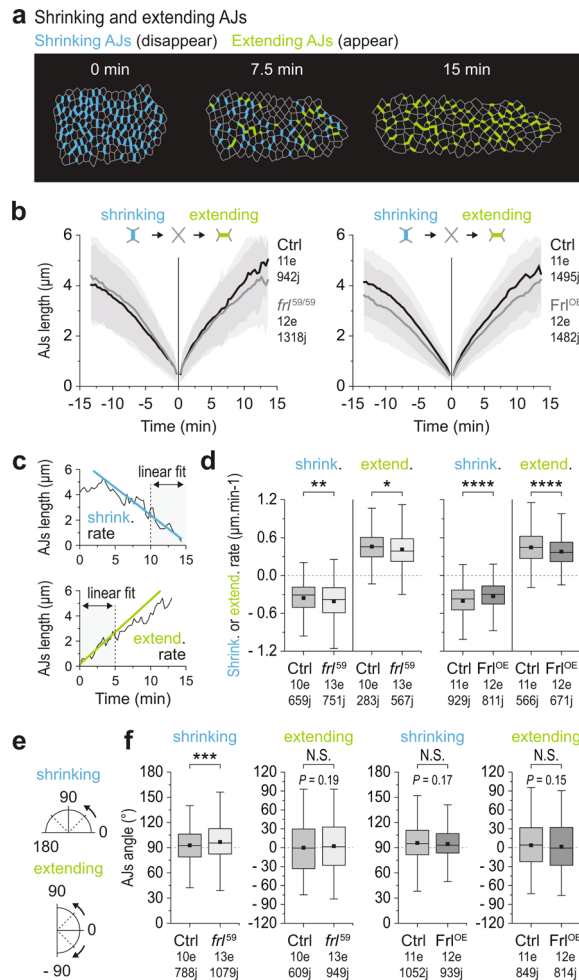
Extended Data Fig. 1 | Quantifying the medio-apical F-Actin dynamics. **a**, Comparison between live (eGFP::UtrCH) and fixed (Phalloidin) F-Actin localization in ectodermal (GBE) and amnirosa cells (DC). **b**, Automatic cell segmentation procedure used to define medio-apical ROIs for quantification (see Methods). Briefly, cell boundaries are detected on the lower junctional plane using a watershed algorithm. The segmented cells are then identified and tracked over time to define ROIs. Finally, these ROIs are shrunk of a few pixels to discard the junctional signal and the medial fluorescence intensities are measured on the max. proj. of the Z-series. **c**, Presentation of the background subtraction procedure (see Methods). The background is evaluated on the lower Z-planes and subtracted from the max. proj. of the Z-series before quantification. Removing the background is critical to properly measure the total amount of fluorescence in the ever-changing apical cell surface (see time shift when comparing the medial F-Actin levels with or without background subtraction). **d**, To quantify the levels of pulsed contractility, we processed single cell profiles using a high-pass Butterworth IIR filter (see Methods). This filter is used to remove low frequency components and have been adjusted to fit the temporality of pulsatility in GBE and DC. Results in **a,c,d** have been systematically observed in 20 independent experiments. Scale bars size is directly indicated on the pictures. Statistical source data are provided in Source Data Extended Data Fig. 1.



Extended Data Fig. 2 | Spatio-temporal tracking of pulses and numerical modeling. **a**, Description of the method used to quantify to pulsatile Rho1 activity without cell segmentation (see Methods and Supplementary Movie 16). Clusters of AniRBD::eGFP signal are detected using a DBSCAN algorithm. These clusters are then converted into surface ROIs using convex hulls and overlapping ROIs tracked over time to follow individual pulses. Filters such as min./max. area or min./max. duration are applied to reduce tracking mistakes. The AniRBD::eGFP pulse amplitude measurements are performed considering the maximum of total fluorescence intensity for each track. **b**, MyoII pulses are automatically detected in time following the derivatives of high-pass filtered total medial MyoII levels (see Methods). Pulse temporal landmarks have been defined as follow: t_i: initial time; td_{max}: max derivative; t_{max}: max amplitude; td_{min}: min derivative; t_f: final time. **c**, MyoII pulses are automatically detected in space by monitoring the centre of mass of the medial sqh::mKate2 signal over time (see Methods and Supplementary Movie 22). The pulse centre used for the KLT analysis is defined by averaging the position of the recorded centre of mass between td_{max} and td_{min} of the pulse. This time interval corresponds to the period during which the apical surface contract during a pulse. **d**, Line plots: Averaged speed towards the pulse according to pulse temporal landmarks (see above) for different distance bins (see legend). The black arrows show the time of maximum speed. **e**, Schematics of the numerical model. The black circle depicts the actomyosin pulse, and arrows depict forces applied to boundary elements. Only a fraction of boundary elements is represented. Results in **a** are representative of 17 independent experiments. Results in **b,c** are representative of 16 independent experiments. Results in **d** are representative of 4 independent experiments. Scale bars size is directly indicated on the pictures. Statistical source data are provided in Source Data Extended Data Fig. 2.



Extended Data Fig. 3 | Control engrailed-GAL4 overexpression and junctional actomyosin quantifications. **a**, Distribution of measured nuclear NLS::RFP fluo. int. and selected threshold to define the control (<475) and engrailed-GAL4 induced NLS::RFP cells (>475). **b**, Box plots: mean medial F-Actin fluo. int. averaged per cell and over time (90 or 120 × 10 sec), normalized to the mean of controls. **c**, Box plots: cell averaged S.D. of high-pass filtered total medial F-Actin (left) fluo. int. and apical cell area (right), normalized to the mean of controls. **d,e**, Box plots: cell averaged mean junctional MyoII (left) and F-Actin (right) intensities in ectodermal (d) or amnioserosa cells (e), normalized to the mean of controls. Quantifications and statistical analysis in **a–e** were carried out using n = the total number of cells gathered from multiple embryos, as indicated below graphs (e = embryos, c = cells). Box plots in **b,c,d,e**: as described in Fig. 1 legend. Statistics in **b,c,d,e**: two-sided Mann-Whitney test, NS: p > 5E-2, *: p < 5E-2, **: p < 5E-3, ***: p < 5E-4, ****: p < 5E-5. Statistical source data are provided in Source Data Extended Data Fig. 3.



Extended Data Fig. 4 | Junctional dynamics in *Frl* loss or gain of function during GBE. **a**, Display of the shrinking and extending AJs in ectodermal cells during GBE, defined respectively as the disappearing and appearing junctions throughout movies duration. **b**, Line plots: averaged AJs length \pm S.D. over time depicting shrinking (before reference time $t = 0$ min) and extending (after reference time $t = 0$ min) junctions. **c**, Line plots: one junction example of shrinking (top) and extending (bottom) AJs and the linear fit method used to extract the shrinking and extending rate. **d**, Box plots: junction shrinking and extending rate in WT vs *frl*^{59/59} (left) or WT vs *Frl*^{OE} (right) ectodermal cells. **e**, Diagrams showing the reference angles used to quantify the shrinking (top) and extending (bottom) junction orientation. **f**, Box plots: junction orientation angle in WT vs *frl*^{59/59} (left) or WT vs *Frl*^{OE} (right) ectodermal cells. Results in **a-f** are representative of 5 (2 control, 3 *frl*^{59/59}) and 5 (3 control, 2 *Frl*^{OE}) independent experiments. Quantifications and statistical analysis in **b,d,f** were carried out using $n =$ the total number of junctions gathered from multiple embryos, as indicated below graphs (e = embryos, j = junctions). Box plots in **d,f**: as described in Fig. 1 legend. Statistics in **d,f**: two-sided Mann-Whitney test, NS: $p > 5E-2$, *: $p < 5E-2$, **: $p < 5E-3$, ***: $p < 5E-4$, ****: $p < 5E-5$. Statistical source data are provided in Source Data Extended Data Fig. 4.

Corresponding author(s): Thomas Lecuit

Last updated by author(s): Mar 11, 2020

Reporting Summary

Nature Research wishes to improve the reproducibility of the work that we publish. This form provides structure for consistency and transparency in reporting. For further information on Nature Research policies, see [Authors & Referees](#) and the [Editorial Policy Checklist](#).

Statistics

For all statistical analyses, confirm that the following items are present in the figure legend, table legend, main text, or Methods section.

n/a Confirmed

- The exact sample size (n) for each experimental group/condition, given as a discrete number and unit of measurement
- A statement on whether measurements were taken from distinct samples or whether the same sample was measured repeatedly
- The statistical test(s) used AND whether they are one- or two-sided
Only common tests should be described solely by name; describe more complex techniques in the Methods section.
- A description of all covariates tested
- A description of any assumptions or corrections, such as tests of normality and adjustment for multiple comparisons
- A full description of the statistical parameters including central tendency (e.g. means) or other basic estimates (e.g. regression coefficient) AND variation (e.g. standard deviation) or associated estimates of uncertainty (e.g. confidence intervals)
- For null hypothesis testing, the test statistic (e.g. F , t , r) with confidence intervals, effect sizes, degrees of freedom and P value noted
Give P values as exact values whenever suitable.
- For Bayesian analysis, information on the choice of priors and Markov chain Monte Carlo settings
- For hierarchical and complex designs, identification of the appropriate level for tests and full reporting of outcomes
- Estimates of effect sizes (e.g. Cohen's d , Pearson's r), indicating how they were calculated

Our web collection on [statistics for biologists](#) contains articles on many of the points above.

Software and code

Policy information about [availability of computer code](#)

Data collection

Image acquisition was performed with the Metamorph (v7.8.4)

Data analysis

Data were analyzed using ImageJ/Fiji 1.52t and Matlab 2015a.

For manuscripts utilizing custom algorithms or software that are central to the research but not yet described in published literature, software must be made available to editors/reviewers. We strongly encourage code deposition in a community repository (e.g. GitHub). See the Nature Research [guidelines for submitting code & software](#) for further information.

Data

Policy information about [availability of data](#)

All manuscripts must include a [data availability statement](#). This statement should provide the following information, where applicable:

- Accession codes, unique identifiers, or web links for publicly available datasets
- A list of figures that have associated raw data
- A description of any restrictions on data availability

The authors declare that the data and the analysis methods supporting the findings of this study are available within the paper and its supplementary information files. Raw image data and code are available upon request.

Field-specific reporting

Please select the one below that is the best fit for your research. If you are not sure, read the appropriate sections before making your selection.

 Life sciences Behavioural & social sciences Ecological, evolutionary & environmental sciences

For a reference copy of the document with all sections, see nature.com/documents/nr-reporting-summary-flat.pdf

Life sciences study design

All studies must disclose on these points even when the disclosure is negative.

Sample size	Sample size (embryos, cells, pulses, junctions) are indicated next to the graphs on the figures. No statistical method was used to predetermine sample size. The sample size was based on previous studies in the field.
Data exclusions	No embryos were excluded from the analysis.
Replication	Quantifications were carried out on a minimum number of 7 embryos from a minimum number of 3 independent experiments (mounting). Consistency across replicates is captured in each experiment by means and standard deviations calculated across multiple replicates. All attempts at replication were successful to the extent reflected in means, data distributions, and statistical tests described in the manuscript.
Randomization	The experiments were not randomized, and the investigators were not blinded to allocation during experiments and outcome assessment. Blinding was not relevant to this study because experimental procedures did not allow randomization.
Blinding	The experiments were not randomized, and the investigators were not blinded to allocation during experiments and outcome assessment. Automatic image analysis provided an objective and unbiased evaluation of phenotypes in most experiments.

Reporting for specific materials, systems and methods

We require information from authors about some types of materials, experimental systems and methods used in many studies. Here, indicate whether each material, system or method listed is relevant to your study. If you are not sure if a list item applies to your research, read the appropriate section before selecting a response.

Materials & experimental systems

n/a	Involved in the study
<input checked="" type="checkbox"/>	Antibodies
<input checked="" type="checkbox"/>	Eukaryotic cell lines
<input checked="" type="checkbox"/>	Palaeontology
<input type="checkbox"/>	Animals and other organisms
<input checked="" type="checkbox"/>	Human research participants
<input checked="" type="checkbox"/>	Clinical data

Methods

n/a	Involved in the study
<input checked="" type="checkbox"/>	ChIP-seq
<input checked="" type="checkbox"/>	Flow cytometry
<input checked="" type="checkbox"/>	MRI-based neuroimaging

Animals and other organisms

Policy information about [studies involving animals](#); [ARRIVE guidelines](#) recommended for reporting animal research

Laboratory animals

Drosophila Melanogaster embryos were used in this study and all experiments were carried out according to Campos-Ortega staging between stage 6 and stage 8. The experimental procedure did not allow identifying the sex of the embryos at the time of the experiment.

Wild animals

The study did not involve wild animals.

Field-collected samples

The study did not involve samples collected from the field.

Ethics oversight

The study did not require ethics oversight.

Note that full information on the approval of the study protocol must also be provided in the manuscript.